 doi:10.20944/preprints202208.0123.v1

Human-in-the-loop optimization of transcranial electrical stimulation effects: a computational perspective based on systems analysis

Yashika Arora[1], Anirban Dutta[2*]

[1] Neuroimaging and Neurospectroscopy, National Brain Research Centre, Gurgaon 122051, India
[2] Neuroengineering and Informatics for Rehabilitation Laboratory, Jacobs School of Medicine & Biomedical Sciences, Department of Biomedical Engineering, University at Buffalo, Buffalo, NY, USA

*** Correspondence:**
Corresponding Author
adutta@case.edu

Keywords: systems analysis; model predictive control; transcranial electrical stimulation; functional near infrared spectroscopy; pupillometry.

Abstract

Individual differences in the responsiveness of the brain to transcranial electrical stimulation (tES) is increasingly demonstrated in large variability in the tES effects. Anatomically detailed computational brain models have been developed to address this variability; however, static brain models are not 'realistic' in accounting for the dynamic state of the brain. Therefore, human-in-the-loop optimization is proposed in this perspective article based on an extensive systems analysis of the tES neurovascular effects. First, modal analysis was conducted using a physiologically detailed neurovascular model that found stable modes in the 0 Hz to 0.05 Hz range for the pathway for vessel response through the smooth muscle cells, measured with functional near-infrared spectroscopy (fNIRS). tES effects in the 0 Hz to 0.05 Hz range can also be measured with functional magnetic resonance imaging (fMRI)-tDCS data with a maximum TR=10sec. Therefore, we investigated an open-source fMRI-tDCS dataset that used a TR=3.36sec. We found that both the anodal tDCS condition and sham tDCS condition had similar Finite Impulse Response at the region of interest underlying the anode and a remote location, which indicated a global hemodynamic effect of sham tDCS beyond the intended transient sensations. Here, transient sensations can have arousal effects on the hemodynamics so we conducted a healthy case series for black box modeling of fNIRS-pupillometry of short-duration tDCS effects. The block exogeneity test rejected the claim that tDCS is not a 1-step Granger-cause of the fNIRS total hemoglobin changes (HbT) and pupil dilation changes ($p<0.05$). Also, grey-box modeling using fNIRS of the tDCS effects in chronic stroke showed HbT response to be significantly different (paired-sample t-test, $p<0.05$) between the ipsilesional and the contralesional hemisphere for primary motor cortex tDCS and cerebellar tDCS which was subserved by the smooth muscle cells. Here, our perspective is that various physiological pathways subserving tES effects can lead to state-trait variability that can be challenging for clinical translation. Therefore, we conducted a case study on human-in-the-loop optimization using our reduced dimension model and a stochastic, derivative-free Covariance Matrix Adaptation Evolution Strategy. Future studies need to investigate human-in-the-loop optimization of tES for reducing inter-subject and intra-subject variability in tES effects.

Preprints (www.preprints.org) | NOT PEER-REVIEWED | Posted: 5 August 2022 doi:10.20944/preprints202208.0123.v1

1 Introduction

Grey-box modeling of the signals from brain computer interfaces, viz. portable brain imaging and pupillometry, can provide causal inference of the impairments in neurological patients [1–3], Alzheimer's Disease and Alzheimer's Disease-Related Dementias [4]. Specifically, evoked brain responses in a multi-modal brain computer interfaces when combined with cognitive, motor, or transcranial electrical stimulation (tES) can enable system analysis and design of the therapeutic intervention with human-in-the-loop optimization [5] using brain-based metrics. Then, multi-modal brain imaging can cross-validate the metrics across different physiological domains. For example, simultaneous functional near-infrared spectroscopy (fNIRS) and electroencephalogram (EEG) can elucidate neurovascular modulation by tES in health and disease [6] that can be dysfunctional post-stroke [7]. Here, transient coupling relation between the changes in EEG power spectrum and fNIRS hemodynamics signals during tES can be monitored using Kalman filter based online parameter estimation of an autoregressive (ARX) model [8]. Then, a grey-box modeling approach [9] can provide physiological insights based on a detailed multi-compartmental neurovascular model incorporating vascular smooth muscle, perivascular space, synaptic space, and astrocyte glial cell. Such computational modeling, when fitted to individual dysfunction, can allow personalized therapeutic interventions, e.g. tES with model predictive control using subject-specific fNIRS based measure of tES evoked blood volume changes (e.g., total hemoglobin concentration changes), called cerebrovascular reactivity (CVR) to tES. However, for model predictive control, computationally expensive physiologically detailed nonlinear model needs to be simplified with an appropriate complexity (Akaike information criterion) for online 'real-time' performance. Here, the simplified model needs to capture the inherent dynamic characteristics of the neurovascular system in forms of natural frequencies and damping factors, e.g., the changes in the dynamic characteristics from the arterioles as they transition into cerebral capillaries with smooth muscle cells replaced by pericytes and mural cells embedded into the endothelial basement membrane in the smaller vessels. Mode decomposition approaches [10],[7], including dynamic mode decomposition [11], can be applied to reduce the complexity of the multi-modal multi-channel data

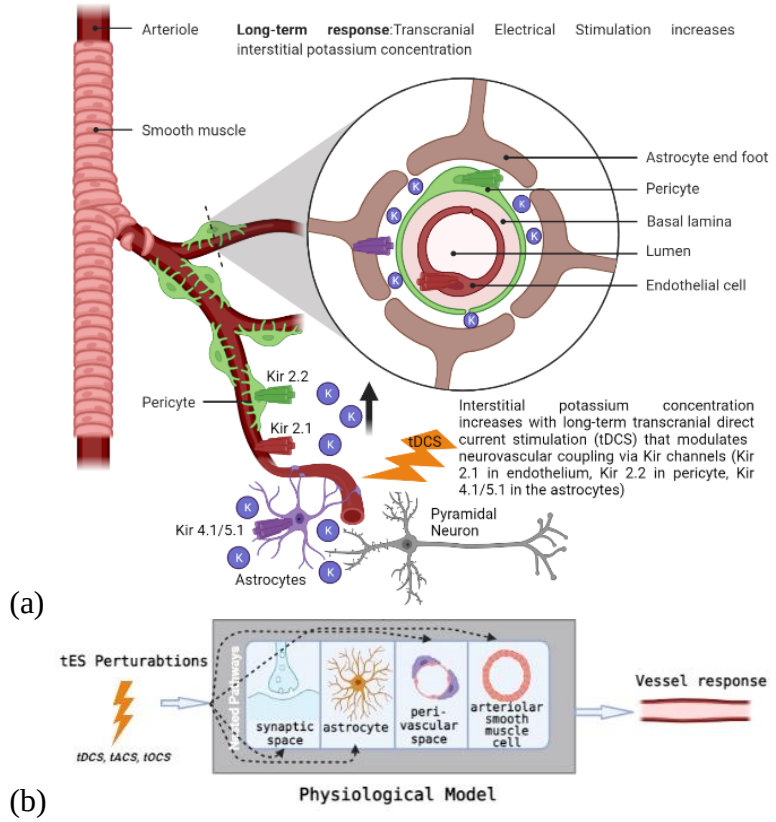

Figure 1: (a) Long-term (≥3min) transcranial electrical stimulation can change the interstitial concentration of potassium that will modulate the neurovascular system's sensitivity via Kir channels. (b) Four compartment lumped physiological model of the neurovascular unit with nested pathways (dashed arrows) that can be perturbed by the tES current density leading to vessel response in terms of diameter changes.

 doi:10.20944/preprints202208.0123.v1

to their dominant features and essential components. Here, experimental data from multi-distance fNIRS probes can capture a combination of vessel oscillations from the pial, penetrating, and precapillary arterioles to the capillaries based on the inter-optode distance and photon migration through the neurovascular tissue determined by the fNIRS optode's point-spread functions. Moreover, cerebrospinal fluid (CSF) pulsatility in the subarachnoid space due to pial vessels can be picked up by the near-infrared backscattering using shorter distance probes; however, delineating different 'dynamic modes' in the fNIRS signal vis-à-vis a mechanistic understanding of subject-specific dysfunction will require physiologically realistic computational model with the inherent dynamic characteristics of the neurovascular system. Various physiologically relevant frequency bands have already been identified in the literature [12], e.g., 0.6–2 Hz and 0.145–0.6 Hz are related to cardiac and respiratory function. Then, 0.052–0.145 Hz is associated with smooth muscle cell activity, while 0.021–0.052 Hz has been proposed to reflect smooth muscle autonomic innervation [12]. Norepinephrine [13] receptors are present on the pial arterial smooth muscle cells [14,15]. In fact, vasomotion can be elicited with a contractile stimulation of single-dose norepinephrine in internal thoracic artery segments [16]. Such evoked responses can provide a biomarker, e.g., vasomotion is associated with endothelial dysfunction [16] and norepinephrine deficiency has been linked to the pathogenesis of the Alzheimer's Disease (AD) that can be related to a reduced vessel pulsatility and amyloid-beta clearance [17] via perivascular pathways [18]. Then, 0.01–0.02Hz oscillations are known to be crucial to support higher oxygen concentration distant from the small vessels [19]. Zhao et al. [20] found a drop in the oscillatory power in the 0.01–0.02Hz frequency band during Mini-Cog assessment for dementia, where this drop was more significant in type 2 diabetes Mellitus (T2DM) than age-matched normoglycemic elderly. Small vessel oscillations support nutrient supply where low-frequency Fahraeus–Lindqvist-driven (not blood pressure-driven) oscillations in the small vessels are crucial [19]. Mechanistic understanding of the cause of diabetic brain fog may be found in terms of the small vessel pulsatility in the 0.01–0.02Hz frequency band and the oxygen diffusion distant from the small vessels [19]. Here, modal analysis can provide the characteristic dynamics of a detailed multi-compartmental neurovascular system from its natural frequencies, mode shapes, and damping factors and develop a simpler mathematical model of the system's behavior for therapeutic intervention with tES. Typically, modal analysis method is prevalently used in structural and fluid mechanics and can be well applied for biomedical system analysis to derive the modal behavior of the output responses.

Investigation of different 'dynamic modes' in the vessel oscillations in health and disease is also crucial since vascular factors are an essential contributor to cerebrovascular disease [21], including a role in mild cognitive impairment and dementia [22], that is predicted to increase to 152 million by 2050 (Alzheimer's Disease International London, UK, 2019). Here, we postulate that tES evoked 'dynamic modes' [7] may be more informative than the resting state ones and tES evoked onset vascular response is partly driven by the arousal effect via the locus coeruleus norepinephrine (LC-NE) system. Transcranial direct current stimulation (tDCS), a tES modality, can perturb the blood vessel and evoke regional cerebral blood flow (CBF) [23]. We found that the CVR to tDCS following the cerebrovascular accident was significantly less in the lesioned hemisphere [24] which was postulated to be related to neurovascular coupling status. Since stroke is a specific vascular risk factor for dementia [25] so the neurovascular coupling status may be relevant [26]. Then, anodal tDCS-induced neuronal excitation causes an energetic depletion that was quantified by ^{31}phosphorus magnetic resonance spectroscopy [27]. Here, tDCS-induced cerebral energy consumption promoted systemic glucose tolerance in a standardized euglycemic-hyperinsulinemic glucose clamp procedure in healthy male volunteers. In fact, tDCS effect may be similar to the cognitive load-led reduction in blood glucose [28] where stressor related norepinephrine release and regulation of astrocytic and neuronal metabolism is relevant [29]. LC-NE network is known to optimize coupling

Preprints (www.preprints.org) | NOT PEER-REVIEWED | Posted: 5 August 2022 doi:10.20944/preprints202208.0123.v1

of cerebral blood volume with oxygen demand [30] that can affect the neurovascular coupling [8],[6]. Then, the vasoconstricting perivascular pathway via norepinephrine [13] receptors on the pial arterial smooth muscle cells [14,15] may be relevant at the onset (<150 sec after tDCS) of tDCS [9],[31]. Then, longer duration (>150 sec) tDCS can modulate the neurovascular coupling [31] and synaptic potentiation which is likely via postsynaptic signaling including nitric oxide and interstitial potassium concentration as shown in Figure 1a.

Smooth muscle autonomic innervation can regulate vascular tone [12]. The autonomic nervous system (ANS) is comprised of sympathetic and parasympathetic nervous system. ANS neurotransmitters are the norepinephrine (NE), adenosine triphosphate (ATP), and Neuropeptide Y (NPY) that function as vasoconstrictors, whereas acetylcholine (Ach) and calcitonin gene-related peptide (CGRP) can mediate vasodilation. Immediate onset effects of tDCS on the blood volume changes (e.g., total hemoglobin concentration changes), including the 'initial dip' [7], may be sub-served by the evoked balance of autonomic effectors including NE and Ach. Here, direct electrical stimulation of noradrenergic axon is possible [13] in addition to arousal effect via the LC-NE system. Since prior works have found coupling between the alpha-band (8–12 Hz) EEG activity and pupil diameter [32] as well as between log (base-10) transformed EEG band-power (0.5-11.25Hz) and fNIRS signal [8]; therefore, we aimed to investigate coupling between the pupil dilation and fNIRS signals during tDCS. Specifically, Granger causality test can be used to assess whether tDCS waveform in a 3-D vector autoregression (VAR) model Granger-causes total hemoglobin changes (i.e., blood volume changes) conditioned on the pupil dilation. This is important since peripheral effect of tDCS on brain circuits involving memory via the ascending fibers of the occipital nerve to the locus coeruleus [33], viz. during cerebellar tDCS [34], can be beneficial in ameliorating cognitive impairment. Then, adrenergic regulation may also be relevant [29] in longer duration (20min) tDCS that can lead to Ca2+ elevations in the astrocytes and a neurometabolic biphasic effect on systemic glucose tolerance [27]. Since pupil dilation is a correlate of Ach and LC-NE activity [35] during arousal; therefore, pupillometry with portable brain imaging and 'short-duration (<150sec)' tES may elucidate the autonomic effectors vis-à-vis CBF [6].

CBF is known to be regulated primarily by three mechanisms, cerebral autoregulation that maintains the CBF under changes in systemic blood pressure; cerebral vasoreactivity that is the response to the arterial CO2 partial pressure changes; and neurometabolic that is the response to the neuronal activity [36]. A recent study [37] showed that the spatial distribution of CBF changes correlated with the tDCS-induced electric field distribution (< 1 V/m) computed using finite element modeling. CBF changes can also be evoked rapidly (<100 ms) with transcranial alternating current stimulation (tACS) at 10-20 Hz; however, at a higher electric field strength (5-20 V/m) [38]. Here, tACS can target neural oscillations [39]; however, rapid changes in the CBF indicate a direct effect of the electric field on the vascular neural network [40]. Brain capillaries act as a neural activity-sensing network that can be perturbed by tES to identify characteristic natural frequencies and damping factors from the resulting dynamics of the metabolic and vascular responses. A multi-scale model will be needed for mechanistic understanding of the metabolic responses, e.g., the computational model by Jolivet et al. [41] that captured the concentration of lactate in neuronal, astrocytic, and extracellular compartments which were coupled as a modulatory feedback [42][43] to neuronal membrane voltage. Then, individual hemodynamic effects, including neurovascular network resonant frequencies, of the tES via various neurovascular pathways need to be investigated using a mechanistic model-based hypothesis testing that is postulated to be subject-specific [44]. Such model-based system analysis is important since mechanistic models will allow human-in-the-loop optimization of tES to enhance its metabolic effects, e.g., in T2DM.

Preprints (www.preprints.org) | NOT PEER-REVIEWED | Posted: 5 August 2022 doi:10.20944/preprints202208.0123.v1

Lumped vessel biomechanics plays an important role in vessel oscillations [31] where CBF can be partly modulated by the balance of autonomic effectors on the vascular tone. However, more detailed grey-box modeling and analysis of the neurovascular coupling system need to include multi-scale vessel biomechanics where small vessels will have different characteristic natural frequencies than the pial vessels. Proximal pial arteries and the descending arteries have the fastest onset time followed by the capillaries (spatiotemporal characteristics of pial, penetrating, and micro-vessels are summarized in Schmid et al. [45]) that can have several modes of oscillations with frequencies ranging from 0.005 to 1 Hz. However, the oscillatory responses can be quite complex due to the interdependence of the nested spatiotemporal dynamics of the pial arteries, descending arteries, and the capillaries. Then, various tES modalities have differences in the temporal profile of the electric current stimulation that may perturb the vessel oscillations differently. In transcranial direct current stimulation (tDCS), the current profile has a monophasic, non-oscillating constant value. In contrast, in transcranial alternating current stimulation (tACS), the oscillating current reverses rhythmically at a specific frequency. So, tACS differs from tDCS in that it provides a mechanism for manipulating intrinsic oscillations through the injection of sinusoidal currents. Then, the other methods are transcranial oscillating current stimulation (tOCS) which uses tDCS to set a baseline to the tACS oscillations, and transcranial random noise stimulation (tRNS) that injects 'noisy' current with bounded stochasticity. Because tES's modulatory effects on blood vessels can be mediated by the neuronal and non-neuronal cells in the neurovascular tissue, a deeper understanding of the signalling pathways will be crucial for human-in-the-loop optimization of the tES effects, including its effects on the vessel oscillations [46]. In this study, human-in-the-loop optimization was performed using a stochastic, derivative-free Covariance Matrix Adaptation Evolution Strategy (CMA-ES) [47] that can be used for non-linear, non-convex optimization problems with noisy measurements (https://cma-es.github.io/).

The next sections of this computational perspective article provide systems analysis of the tES effects that are relevant for model based human-in-the-loop optimization. Section 2 presents the modal analysis of our published physiologically detailed neurovascular model [31] to elucidate the oscillatory responsiveness of the vasculature including to cardiac and respiratory rhythms. Then, Section 3 presents nonparametric impulse response estimation of the neurovascular system (0 Hz to 0.05 Hz range) from the published open-source fMRI-tDCS data to elucidate the tDCS effects on the Blood Oxygen Level Dependent signals in healthy individuals. Section 4 presented grey-box modeling of fNIRS of tDCS effects in a chronic stroke case series to elucidate the role of diseased state on the neurovascular system. Here, an initial dip in blood volume or vasoconstriction following tDCS perturbation has been found in chronic stroke that necessitated the study of the role of tDCS evoked arousal in health and disease. In Section 5, we performed black box modeling of prefrontal fNIRS-pupillometry of short-duration frontal tDCS effects to elucidate the effects of tDCS evoked arousal on hemodynamics in healthy

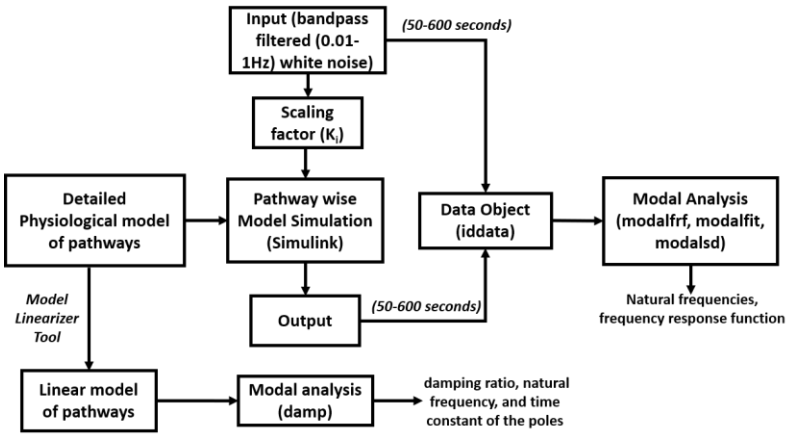

Figure 2: Modal analysis approach used for evaluating the physiological model using Matlab and Simulink (Mathworks Inc., USA).

Preprints (www.preprints.org) | NOT PEER-REVIEWED | Posted: 5 August 2022 doi:10.20944/preprints202208.0123.v1

individuals. Here, the variability in the tDCS effects even in healthy individuals, possibly state-trait variability that can be challenging for clinical translation, motivated feasibility testing of human-in-the-loop optimization for reduced dimension model (8 poles, 2 zeros [31]) predictive control of tES evoked HbT in a healthy individual that is presented in the Section 6.

In Section 2, in order to estimate the mechanistic aspects of the tES effects, we used a mathematical model based on neurovascular tissue physiology of the vascular response through various pathways that are susceptible to the electric field as shown in Figure 1. The simulation model included four compartments based on published literature where the tES current density perturbed synaptic potassium released from active neurons for the Pathway 1, astrocytic transmembrane current for the Pathway 2, perivascular potassium concentration for the Pathway 3, and voltage-gated ion channel current on the SMC for the Pathway 4. The implementation of the detailed model is presented in Yashika et al. [31]. The physiologically detailed models were simulated using the 'ode23tb' solver in Simulink (MathWorks, Inc., USA). Prior work showed that the models captured the interactions between the potassium dynamics and the calcium dynamics in the perivascular space [6]. In this computational perspective article, we performed modal analysis based on the work flow shown in Figure 2 using Matlab and Simulink packages (Mathworks, Inc., USA).

2 Modal analysis of the physiologically detailed neurovascular model

In this study, we used modal analysis approach to analyze the physiologically detailed neurovascular unit (NVU) model for evaluating oscillatory modes that may be perturbed with tACS. The physiological model considered the lumped neurovascular system of vascular smooth muscle (SMC) space, perivascular space, synaptic space, and the astrocyte space; and captured the tES induced direct and indirect vascular responses. The detailed physiological NVU model has been shown to simulate vessel oscillations in the range of 0.05–0.2 Hz governed by the interactions between the Kir 2.1 channels on the endothelium and the Kir 2.2 channels on the pericytes [6],[48]. For modal analysis, we applied ten tES perturbations which were bandpass filtered (0.01-1 Hz) white noise inputs of 600 seconds to the four physiologically constrained NVU pathways as shown in Figure 2 (equations are presented in the supplementary materials of Yashika et al. [31]). The input and the output time series were stored using a time-domain data object ('iddata' in MATLAB, MathWorks, Inc., USA). We excluded the initial 50 seconds of the transient response in the time series data for modal analysis. We used modal analysis functions: 'modalfrf' to determine frequency-response functions for modal analysis, 'modalfit' to determine modal parameters from the frequency-response functions, and 'modalsd' to generate a stabilization diagram for modal analysis on the data object in Matlab (MathWorks, Inc., USA). First, the frequency response functions for the four tES pathways of the NVU system were found using 'modalfrf' for a sample rate of 10 samples per second (10 Hz), where the noise was assumed to be uncorrelated with the input signals. Then, the natural frequencies of the

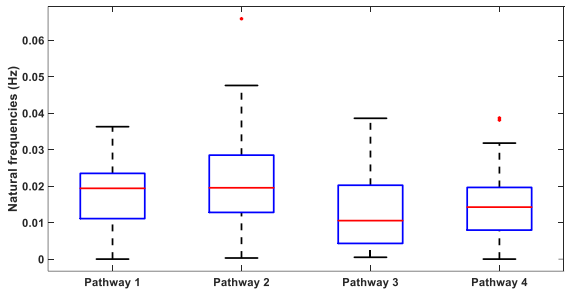

Figure 3: Boxplot of the natural frequencies in the physiological frequency range of 0.01-0.2 Hz obtained through modal analysis for the four tES perturbation model pathways. On each box, the central mark indicates the median, and the bottom and top edges of the box indicate the 25th and 75th percentiles, respectively. The whiskers extend to the most extreme data points not considered outliers, and the outliers are plotted individually using the red '+' symbol.

 doi:10.20944/preprints202208.0123.v1

four tES pathways for the NVU system were found from the frequency-response using the 'peak-picking' method (a fast and straightforward procedure for identifying peaks in the frequency response functions) available in the 'modalfit' function in the physiological frequency range of 0.01-0.2 Hz. Then, a single set of modal parameters were generated using the least-squares complex exponential (LSCE) algorithm by analyzing multiple response signals simultaneously in 'modalsd.' Here, a stabilization diagram is used to identify the physical modes by examining the stability of poles as the number of modes increases. Then, the linear model of the four physiologically detailed tES pathways in the NVU was found using the Model Linearizer tool in the Simulink (MathWorks, Inc., USA) linear analysis package. The damping ratio, natural frequency, and the time constant of the poles were obtained using the 'damp' function from the linear model system.

Table S1 (Supplementary materials: Modal analysis of the physiologically detailed neurovascular model) lists the natural frequencies in the physiological frequency range of 0.01-0.2 Hz obtained using the 'peak-picking' algorithm following the modal analysis of the physiologically detailed non-linear model of the four tES perturbation pathways using ten different seeds for the white Gaussian noise. The 'peak-picking' method is a local single-degree-of-freedom method where the peaks for each mode are considered independently. Here, the natural frequencies across all the four tES perturbation pathways were found in the physiological frequency range of 0.01-0.2 Hz. Figure 3 depicts the boxplot of these natural frequencies within 0.01-0.2 Hz across ten different runs (with different seed – see Table 1) of the modal analysis that were found to be comparable for the four tES perturbation pathways, Pathway 1: tES perturbing vessel response through synaptic potassium pathway, Pathway 2: tES perturbing vessel response through the astrocytic pathway, Pathway 3: tES perturbing vessel response through perivascular potassium pathway, and Pathway 4: tES perturbing vessel response through the SMC pathway. We also applied a global multiple-degree-of-freedom method, LSCE, where the parameters for all modes were estimated simultaneously from multiple frequency-response functions. Figure 4 shows the stabilization diagrams and output of the natural frequencies of the poles that were stable in frequency, which were found for lower (<0.2 Hz) frequencies mainly for Pathway 4 and for higher (>0.2 Hz) frequencies mainly for Pathways 2 and 3. Here, many stable modes were found near 1 Hz mainly for tES perturbation Pathways 2 and 3. Then, stable modes in the physiological frequency range of 0.01-0.2 Hz were mainly for Pathway 4 that led to comparable natural frequencies from the modal analysis (see Figure 3) for the four nested tES perturbation pathways where the Pathway 4 is the last for the vessel response (see Figure 1b). The poles and the damping parameters associated with the linearized models of the four tES perturbation pathways are listed in the Table S2 (Supplementary materials: Modal analysis of the physiologically detailed neurovascular model).

Our results provided a mechanistic understanding of the four physiologically detailed tES pathways in the NVU in terms of their frequency-response functions [46]. Specifically, stable modes (see Figure 4) were found in the 0 Hz to 0.05 Hz range in tES Pathway 4 which may be leveraged to develop tES interventions perturbing vessel response via the SMC pathway including diffusing nitric oxide from postsynaptic signalling. Vascular factors contribute to cerebrovascular disease and mild cognitive impairment and dementia [22], which are predicted to affect 152 million people by 2050 (Alzheimer's Disease International London, UK, 2019). Various physiologically relevant frequency bands have already been identified in the literature: 0.6–2 Hz and 0.145–0.6 Hz are related to cardiac and respiratory function, respectively, 0.052–0.145 Hz is associated with smooth muscle cell activity, and 0.021–0.052 Hz may reflect smooth muscle cell autonomic innervation [12]. Then, many stable modes (see Figure 4) were found near 1 Hz for tES Pathways 2 and 3, which may be leveraged to develop tES interventions perturbing vessel response through the astrocytic and perivascular potassium pathways. Here, increases in interstitial potassium concentration can modulate the

Preprints (www.preprints.org) | NOT PEER-REVIEWED | Posted: 5 August 2022 doi:10.20944/preprints202208.0123.v1

neurovascular coupling [31] which is likely to change the transfer function model including its steady state gain via Kir channels [49]. In a computational modeling study within the frequency range of 0.1 Hz to 10 Hz, Yashika et al. [46] found that the vessel oscillations were more sensitive to transcranial oscillating current stimulation than to the transcranial alternating current stimulation, and entrainment effects were more pronounced for lower frequencies. Here, Kir 2.1 channels on the endothelium and Kir 2.2 channels on the pericytes can modulate [6],[48] the neurovascular coupling, as shown in Figure 1(a), which may have a therapeutic potential in aging and Alzheimer's disease [50]. Therefore, investigation of the tES modulation of neurovascular coupling and the CBF role in facilitating neural processing is crucial [51]. Here, prior works [8],[7],[52] have found that tDCS can change the neurovascular coupling status, which may be mediated by the Kir potassium channels in the mural cells [6], thereby changing the neurovascular system's sensitivity leading to aftereffects. Such modulation of the neurovascular system's sensitivity will change the transfer function (see Figure 1b) from the tES current density (input) leading to vessel response in terms of diameter changes (output) which can be found by tracking the steady state gain, e.g., using Kalman filter based online parameter estimation of an ARX model [8]. Then, short-term (<150sec) tDCS can affect the hemodynamic response [9], including the postulated norepinephrine [33] vasoconstricting perivascular pathway vis-à-vis 'initial dip' [6]. Since we found stable modes in the 0 Hz to 0.05 Hz range for the Pathway 4 (tES perturbing vessel response through the SMC pathway) with the Nyquist frequency at 0.1Hz so a maximum TR=10sec for the functional magnetic resonance imaging (fMRI)-tDCS studies is feasible. Therefore, we investigated an open-source fMRI-tDCS dataset [53] that used a TR=3.36sec and captured 0.052–0.145 Hz associated with smooth muscle cell activity, including 'initial dip' that is postulated via norepinephrine receptors on the pial arterial SMCs [14,15] that can modulate hemodynamics (from arterioles as they transition into capillaries).

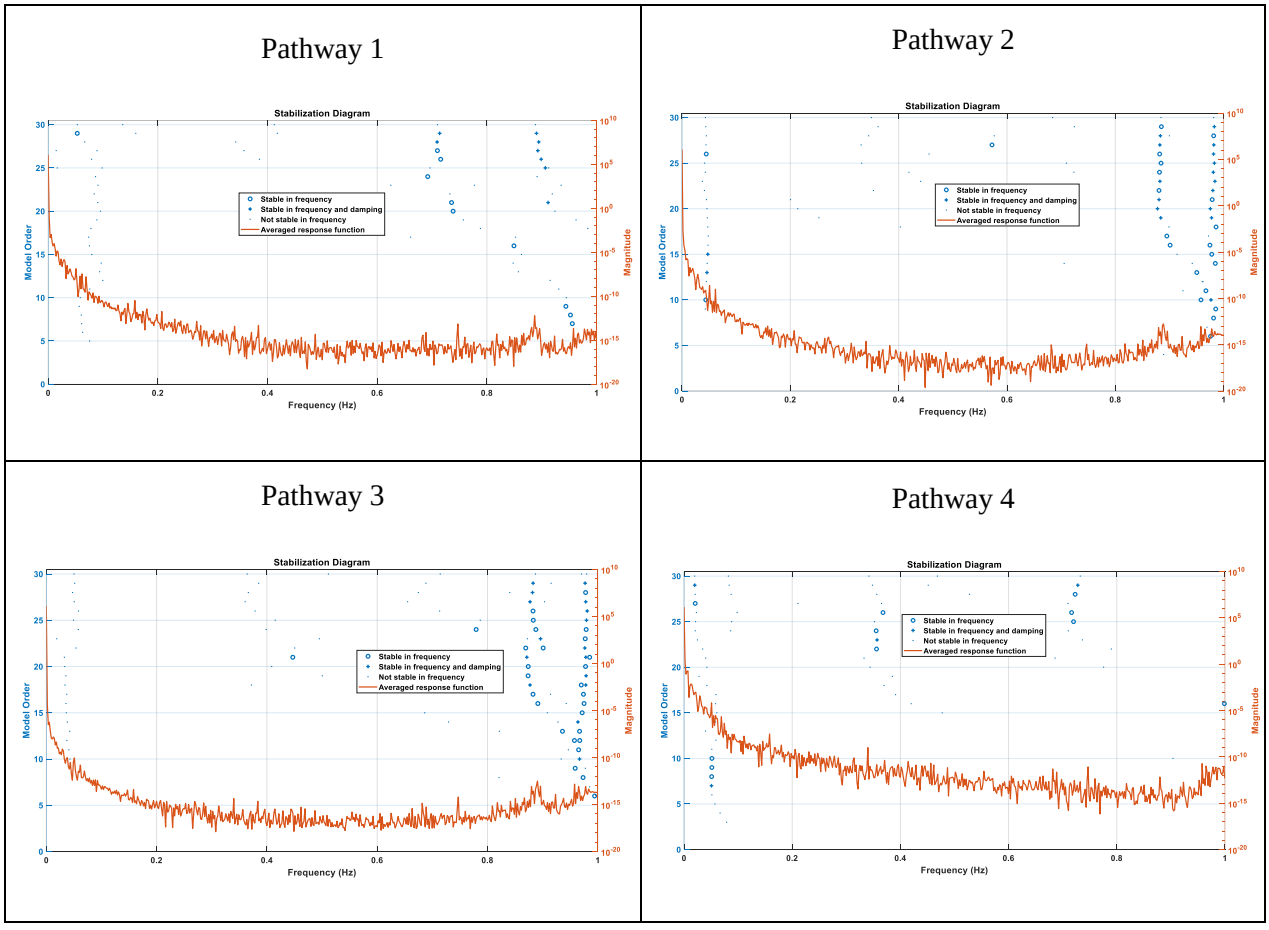

Preprints (www.preprints.org) | NOT PEER-REVIEWED | Posted: 5 August 2022 doi:10.20944/preprints202208.0123.v1

Figure 4: Stabilization diagrams obtained for the four tES perturbation pathways

3 Nonparametric impulse response estimation from fMRI-tDCS data

Ekhtiari and colleagues [54] recently published a checklist for assessing the methodological quality of concurrent transcranial electrical stimulation (tES)-functional magnetic resonance imaging (fMRI) studies; however, the protocol did not elaborate on the methods for separating tES effect on the neuronal activation from the effect on the neurovascular coupling [9], i.e., the hemodynamic response function (HRF). Here, mapping of the tES stimulus-related Blood Oxygen Level Dependent (BOLD) signals measured using fMRI is usually achieved by fitting a general linear model (GLM) to the time course with a pre-specified canonical HRF model, e.g., double-gamma function [55]. Such a canonical HRF univariate model [55] with a single dilation parameter limits physiological interpretability of the neurovascular coupling, which is crucial since tES has been shown to affect the neurovascular coupling in health [8] and disease (e.g., post-stroke [7]) based on the electric field distribution [9]. Spatial localization of HRF has been proposed by Vincent et al. [56] that addresses HRF recovery and localization of the cerebral activity using a black-box Finite Impulse Response (FIR) and temporally regularized FIR models. Yashika et al. [9] published a biophysically informed neurovascular coupling model to capture the hemodynamic response to tES based on fNIRS. Yashika et al. [9] addressed the challenge to find a trade-off between estimation bias and overfitting to fNIRS data by reducing the degrees of freedom in a grey-box model. Grey-box modeling can also be applied to BOLD data for HRF recovery, e.g., one HRF per voxel, which can be used on either volume-based data sets or on data projected onto the cortical surface to reduce the computational needs for inference [56]. Here, the solution with the best fit to the electric field distribution, i.e., the source signal, can be selected using a cost function with regularization in the tES-fMRI studies.

In this paper, we used a nonparametric impulse response estimation of the HRF from an open-source fMRI-tDCS dataset [53] and compared that with the canonical HRF to elucidate tES effects on the temporal profile of the HRF. Figure S1(supplementary materials: Nonparametric impulse response estimation from fMRI-tDCS data) shows the postulated mechanism of the onset response via perivascular nerves and Figure S2 shows the electrical field distribution for 2mA tDCS with FC5 (anodal electrode) and FP2 (cathodal electrode) computed with the ROAST package [57] for the open-source tES-fMRI dataset [53]. Then, Figure 5(a) shows the functional sensitivity metrics calculated using the open-source code and data from the tES-fMRI dataset [53], where anodal tDCS (figure legend: anodal) led to a shift to a higher t-score (first row of Figure 5(a)). Here, the No-tDCS and the Sham-tDCS conditions resulted in a similar HRF temporal profile different from the anodal tDCS condition based on the canonical HRF model. At the same time, the width of the frequency distributions (second row of Figure 5(a)) remained similar across conditions (figure legends: Sham for sham-tDCS, No for no-tDCS conditions), reflecting similar field inhomogeneity. We applied HRF estimation using the rsHRF toolbox[58] that elucidated the effects of anodal tDCS at four ROIs in the grey matter. Figure 5(b) shows that the canonical HRF with time & dispersion derivatives primarily captured the tES effects on the magnitude of the main response and the magnitude of undershoot. In contrast, the FIR model captured the impact on the whole temporal profile of the HRF. Here, we observed that both the anodal tDCS condition and sham tDCS condition had similar FIR at the FC5 (anodal electrode) and PZ (remote location) ROIs based on the nonparametric impulse response estimation that captured the onset response to tDCS in both the conditions which was found to be different from the no-tDCS condition. For the FP2 (cathodal electrode) ROI, the FIR-based HRFs differed across all conditions, specifically anodal tDCS and sham tDCS conditions. Figure 6 shows an estimation of the probability density function across all the voxels for the height parameter of the HRF found using the open-source rsHRF toolbox [58]. The No-tDCS condition

Preprints (www.preprints.org) | NOT PEER-REVIEWED | Posted: 5 August 2022 doi:10.20944/preprints202208.0123.v1

shown with red color resulted in a higher expectation of a lower height HRF parameter than the Sham-tDCS (green color) and the Anodal-tDCS (blue color) conditions from canonical HRF with time & dispersion derivatives as well as finite impulse response model. Here, the Sham-tDCS (green color) and the Anodal-tDCS (blue color) conditions shifted the expectation toward a higher HRF height parameter.

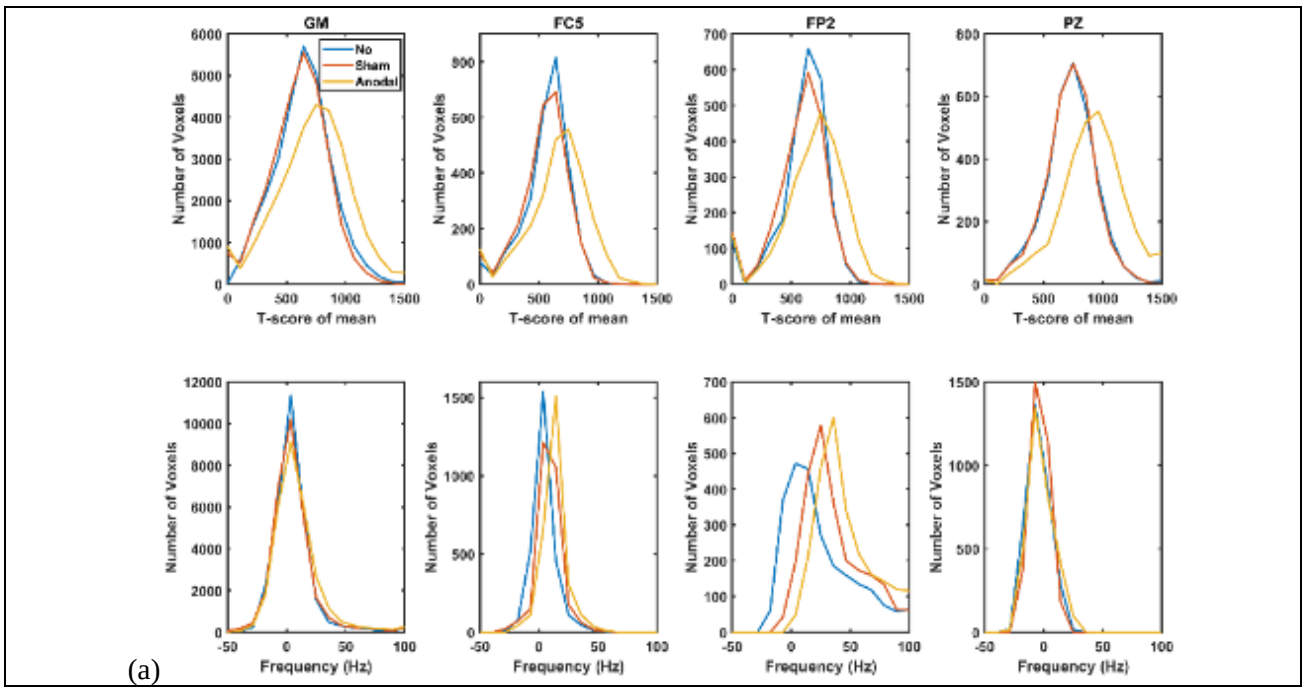

(a)

Preprints (www.preprints.org) | NOT PEER-REVIEWED | Posted: 5 August 2022 doi:10.20944/preprints202208.0123.v1

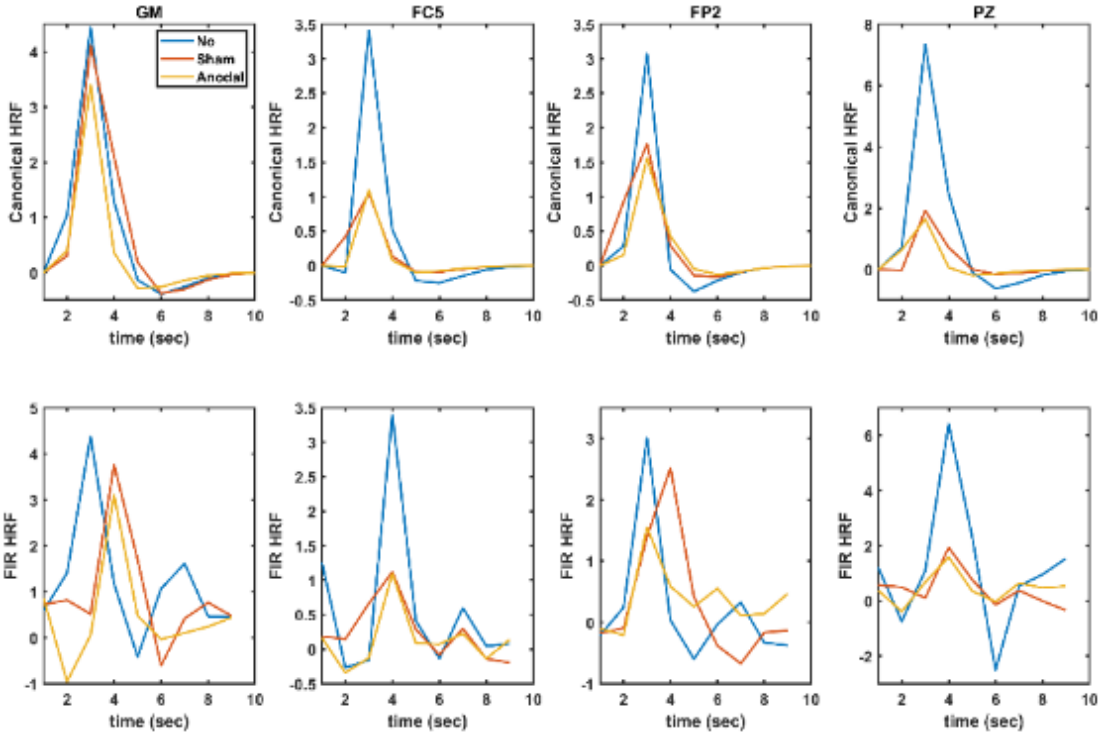

(b)

Figure 5: (a) Functional sensitivity metrics: top row shows the t-score of the mean in the grey matter (GM) and the grey matter ROIs, FC5 (anodal electrode), FP2 (cathodal electrode), PZ (remote location) while the bottom row shows the corresponding offset frequency (in Hz) to capture field inhomogeneity. (b) Estimated hemodynamic response function (HRF) in the grey matter (GM) and the grey matter ROIs, FC5 (anodal electrode), FP2 (cathodal electrode), PZ (remote location) where the top row shows the results using canonical HRF with time & dispersion derivatives while the bottom row shows the results using a finite impulse response (FIR) model. Figure legends: No means no-tDCS condition, Sham means Sham-tDCS condition, Anodal means Anodal-tDCS condition.

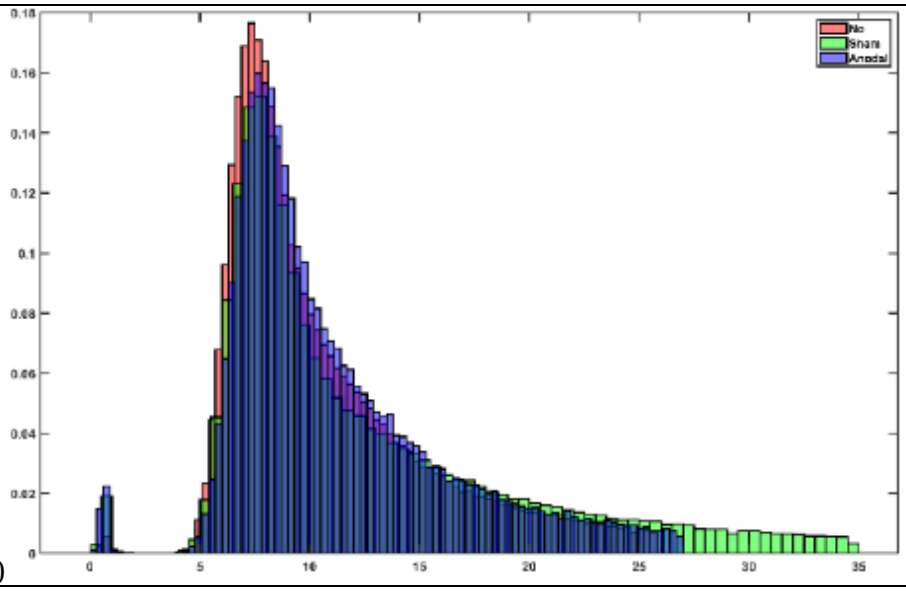

(a)

Preprints (www.preprints.org) | NOT PEER-REVIEWED | Posted: 5 August 2022 doi:10.20944/preprints202208.0123.v1

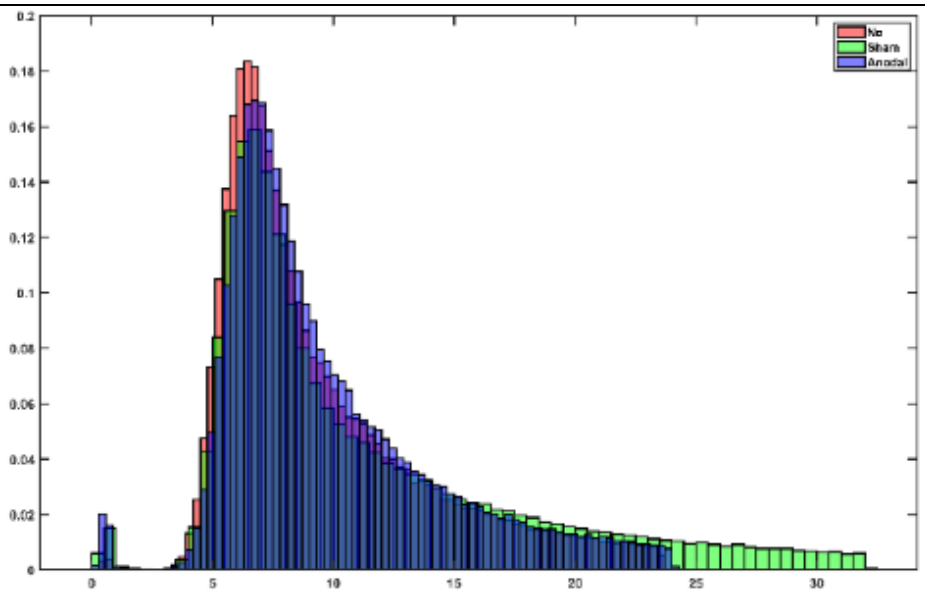

(b)

Figure 6: (a) An estimation of the probability density function across all the voxels for the height parameter (in the x-axis) of the HRF using canonical HRF with time & dispersion derivatives. (b) An estimation of the probability density function across all the voxels for the height parameter (in the x-axis) of the HRF using finite impulse response model. Red: no-tDCS, Green: sham-tDCS, Blue: anodal-tDCS.

Our computational modeling study based on fMRI-tDCS dataset [53] found that both the anodal tDCS condition and sham tDCS condition had similar FIR at the FC5 (anodal electrode) and PZ (remote location) ROIs based on the nonparametric impulse response estimation. Then, for the FP2 (cathodal electrode) ROI, the FIR based HRFs were different across all conditions, specifically anodal tDCS and sham tDCS conditions. Here, it is postulated that the modulation of neurovascular tissue under anode is different than cathode due to difference in the current flow direction that can lead to different local modulation of cortical inhibitory circuits, stimulation of the perivascular nerves and astrocytes (discussed in Yashika et al. [31] and shown in Figure 1b), and their interaction with the electrical communication in the arterial wall [59]. In fact, the ipsilesional hemisphere in chronic stroke can be discriminated based on the tES evoked brain responses [52] that needs further investigation using grey-box modeling approaches [31] – presented next.

Preprints (www.preprints.org) | NOT PEER-REVIEWED | Posted: 5 August 2022 doi:10.20944/preprints202208.0123.v1

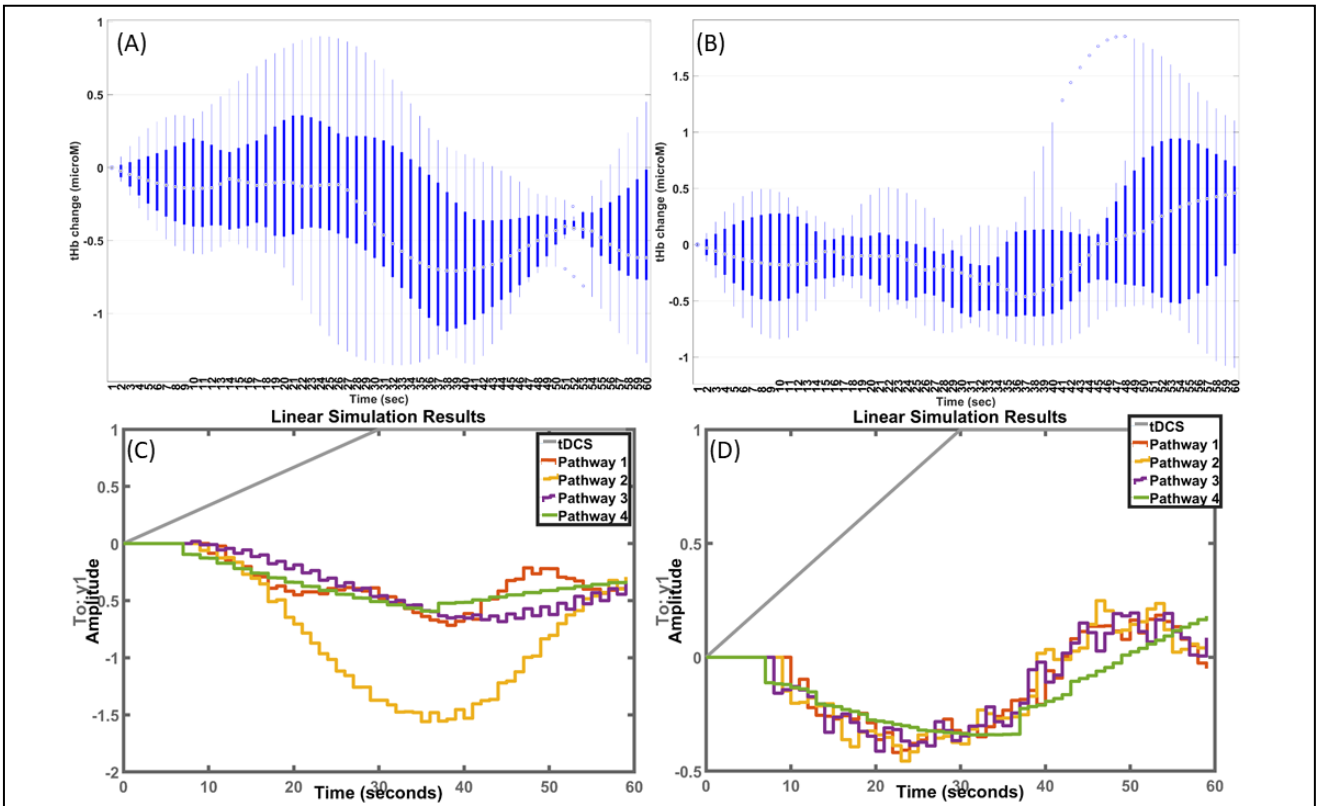

Figure 7: Box-plot of HbT (μM) time-series for 0-60sec of M1 tDCS (0-30sec ramp-up and 30-60sec steady-state) are shown at the ipsilesional (A) and the contralesional (B) hemispheres. Four pathways fitted to fNIRS HbT time-series data at ipsilesional (C) and contralesional (D) hemispheres are also shown.

4 Grey-box modeling of fNIRS of tDCS effects – a chronic stroke case series

In this study, we aimed to compare the cerebellar tDCS evoked fNIRS HbT response with primary motor cortex (M1) tDCS evoked fNIRS HbT response at the lesional and the non-lesional hemispheres in chronic ischemic stroke. Prior works in healthy subjects have shown that tDCS-induced excitability changes in the left M1 correlated with the CBF changes in the left sensorimotor region; however, tDCS-induced alterations in CBF could only partially account for cortical excitability changes [37]. Therefore, although CBF changes were likely evoked by the electric field; however, CBF changes did not completely account for the cortical excitability related neuroplastic changes and its variability [60]. Here, longer plasticity-inducing tDCS is postulated to result in complex bidirectional communication in the neurovascular unit (NVU) [61,62] vis-à-vis to cortical excitability changes which could only be partially accounted for by CBF changes [60]. Therefore, it is important to investigate the underlying mechanism of the hemodynamic response to tDCS-induced electric field in the neurovascular brain tissue, i.e., CVR to tDCS [62], in health and disease.

In healthy tissue, CVR is a compensatory mechanism where blood vessels respond to the vasoactive stimulus from tES that can be related to the neurovascular coupling (NVC) [63]. This capacity of the blood vessels to dilate in response to the vasoactive stimulus can be hampered in various cerebrovascular diseases including chronic stroke [64,65]. In this study, we investigated CVR during tDCS based on grey-box linear systems analysis [31]. Here, completely data-driven black-box systems approaches can provide a correlate of neural and hemodynamic response at an abstract level

Preprints (www.preprints.org) | NOT PEER-REVIEWED | Posted: 5 August 2022 doi:10.20944/preprints202208.0123.v1

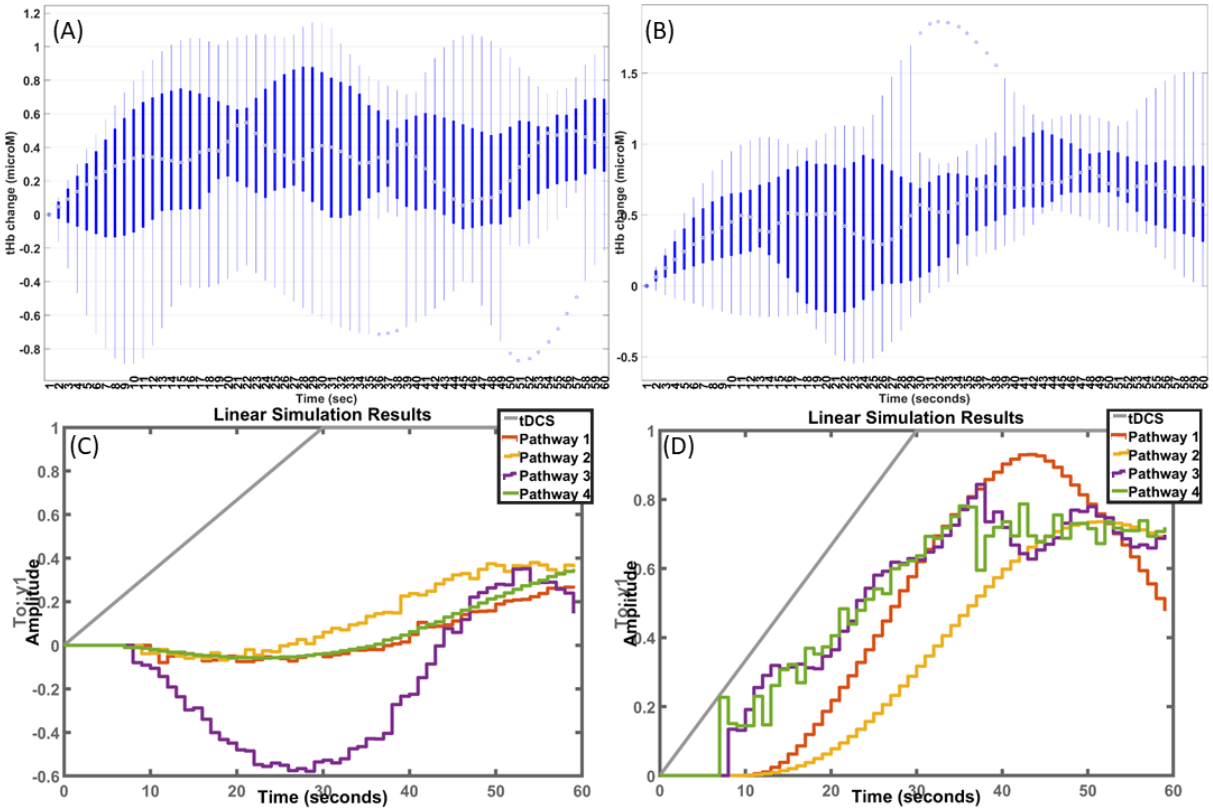

Figure 8: Box-plot of HbT (microM) time-series for 0-60sec of ctDCS (0-30sec ramp-up and 30-60sec steady-state) are shown at the ipsilesional (A) and the contralesional (B) hemispheres. Four pathways fitted to fNIRS HbT time-series data at ipsilesional (C) and contralesional (D) hemispheres are also shown.

under the assumption of NVC at the cellular level. However, these black-box system approaches do not aim to explicitly capture the underlying mechanisms of action. Considering the evidence of modulatory consequences of tDCS on blood vessels that can be via neuronal and non-neuronal cells [66], a deeper understanding of the signaling pathways is important for a mechanistic understanding [6]. Figure 1b shows the four pathways that were physiologically modeled in our prior work [31].

(a) Pathway 1: Synaptic Potassium → vessel circumference

(b) Pathway 2: Astrocytic Current channel → vessel circumference

(c) Pathway 3: Perivascular Potassium → vessel circumference

(d) Pathway 4: Smooth muscle cell → vessel circumference

Retrospective data [34] from a convenience sample of 6 male chronic (>6 months' post-stroke) ischemic stroke subjects who volunteered for the cerebellar tDCS (ctDCS) study are listed in Table 1. T1-weighted MRI was available from All India Institute of Medical Sciences New Delhi, India, and we selected chronic stroke survivors with cerebral lesions but with an intact cerebellum. Written informed consent was obtained from each subject, and the multi-center research protocol was approved by the All India Institute of Medical Sciences, New Delhi, India Institutional Review Board (IEC-129/07.04.2017), and Indian Institute of Technology Gandhinagar, India Institutional Review Board (IEC/2019-20/4/UL/046). Retrospective data [7] from 4 chronic (>6 months) ischemic stroke survivors (1 female) were used for the M1 tDCS analysis, as listed in Table 1.

Preprints (www.preprints.org) | NOT PEER-REVIEWED | Posted: 5 August 2022 doi:10.20944/preprints202208.0123.v1

M1 tDCS was delivered with the anode (SPONSTIM-8, Neuroelectrics, Spain) placed at Cz (international 10–20 system of scalp sites [67]) and the cathode (SPONSTIM-25, Neuroelectrics, Spain) over left supraorbital notch which was conducted at anode current density of 0.526 A/m^2. Cerebellar tDCS (ctDCS) was delivered at PO9h – PO10h (international 10–05 system of scalp sites [67]) with a 3.14cm^2 (PISTIM, Neuroelectrics, Spain) circular anode placed at the contra-lesional side, and the cathode (PISTIM, Neuroelectrics, Spain) was placed at the ipsi-lesional side at higher current density of 6.4 A/m^2. With 0.526 A/m^2, M1 tDCS was postulated to affect the neurovascular tissue mainly at the surface of the cortex while with 6.4 A/m^2, focal ctDCS was postulated to reach deep dentate nuclei of the cerebellum [68] and affect neurovascular tissue at the M1 region via cerebrocerebellar connections. Therefore, fNIRS signal was sampled at 10Hz and analyzed from the M1 region with the source (760/850 nm) placed at the Cz and the detectors placed at FC1, FC2, CP1, CP2 (~2.5cm inter-optode distance) in case of M1 tDCS study. In case of ctDCS study, the detector was placed at Cz and the sources (760/850 nm) were placed at FC3, FC4, CP3, CP4 (~3.5cm inter-optode distance). Computational head modeling for tES current density distribution was performed in ROAST [57] and the fNIRS sensitivity analysis was performed in AtlasViewer [69]. Motion artifact detection and correction was performed using combined spline interpolation and Savitzky-Golay filtering [70] in HOMER3 (https://github.com/BUNPC/Homer3), which is an open-source software in Matlab (Mathworks Inc., USA). Then, modified Beer-Lambert law was used to convert the detectors' raw optical data into optical density. Then, the conversion of optical density to changes in HbT was performed followed by downsampling to 1Hz.

Table 1: Post-stroke subject characteristics and the tDCS target

Name	Age (years)	Gender	Post Stroke Period (years)	Affected Hemisphere (Middle Cerebral Artery Stroke)	tDCS target
P1	44	Male	2	Left	cerebellar
P2	53	Male	3	Left	cerebellar
P3	40	Male	1	Right	cerebellar
P4	38	Male	1	Left	cerebellar
P5	32	Male	1	Left	cerebellar
P6	50	Male	2	Right	cerebellar
P7	31	Male	6	Right	M1
P8	63	Male	5	Left	M1
P9	73	Male	4	Left	M1
P10	76	Female	5	Right	M1

Preprints (www.preprints.org) | NOT PEER-REVIEWED | Posted: 5 August 2022 doi:10.20944/preprints202208.0123.v1

The study used a physiologically constrained linear model [31] to track the HbT changes due to acute (0-60sec: 0-30sec ramp-up and 30-60sec steady-state tDCS) effects of the tDCS current density on the neurovascular tissue. Induced current density in the ohmic head model was assumed to have a vasoactive influence via a linear transfer function mapping to the vasoactive signal. The process of transforming tDCS current density to vasoactive signal was represented by a first-order linear filter, $v(s) = \frac{K}{s/\tau+1} J_{tdcs}$, where K is the gain mapping the current density at the electrode-skin interface (J_{tdcs}) to that at the neurovascular tissue, and τ is the time constant to the vasoactive ($v(s)$) signal (in s-domain) [71]. Physiologically detailed healthy NVC model from published literature were simulated using ODE23TB solver in Simulink (Mathworks, Inc., USA) as detailed in Arora et al. [31]. Then, model reduction of the four pathways from physiologically detailed healthy NVC model was performed using the Simulink (Mathworks, Inc., USA) linear analysis tool. This tool

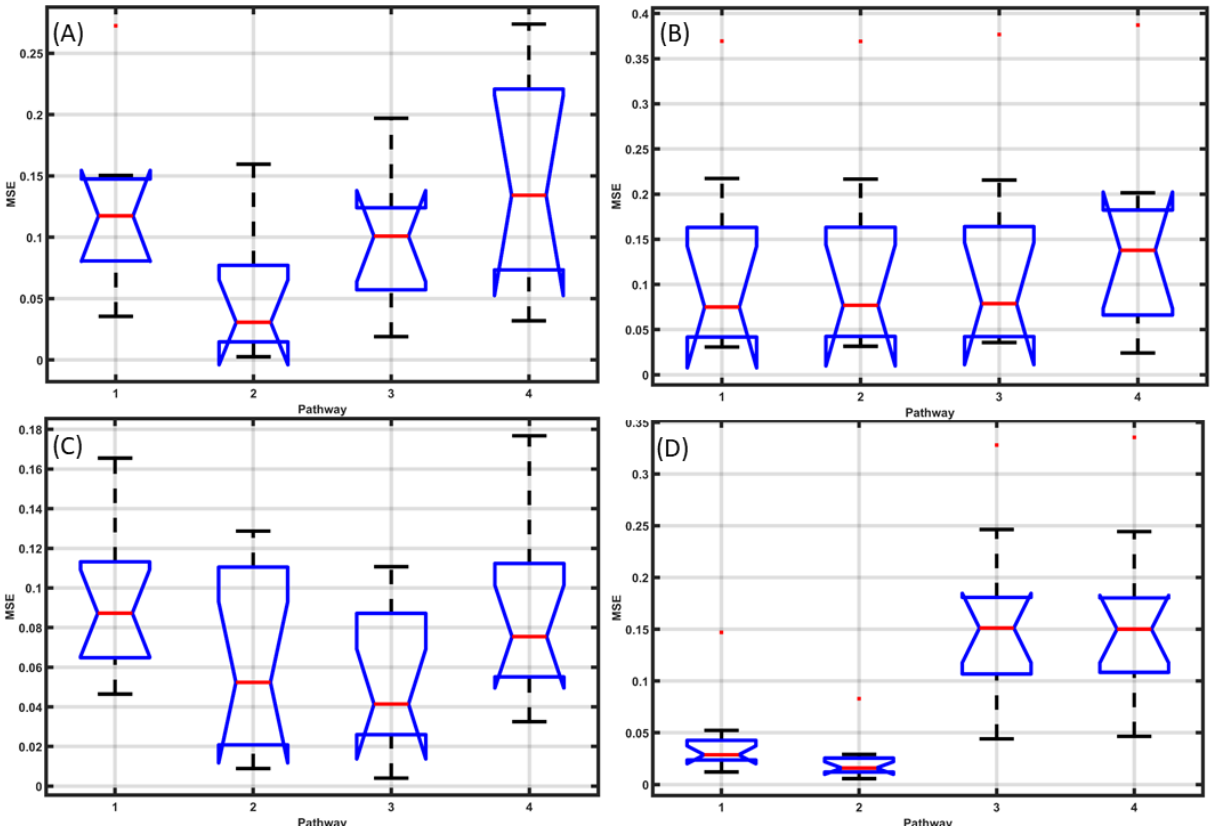

Figure 9: Mean Squared Error (MSE) with M1 tDCS for HbT at the ipsilesional (A) and the contralesional (B) hemispheres. MSE with ctDCS for HbT at the ipsilesional (C) and the contralesional (D) hemispheres.

allowed linearization of nonlinear model at the baseline operating point of the physiologically detailed NVC model. Therefore, the linearized grey-box model was constrained by the individual physiology of the respective four pathways from physiologically detailed healthy NVC model published earlier [31]. Then, the values of the free parameters (poles and zeros) of the grey-box linear model were updated using the "Refine Existing Model" approach in the System Identification toolbox (Mathworks, Inc., USA) to fit to the experimental pathological fNIRS HbT changes (0-60sec) to tDCS in chronic stroke survivors.

Preprints (www.preprints.org) | NOT PEER-REVIEWED | Posted: 5 August 2022 doi:10.20944/preprints202208.0123.v1

After minimizing the mean squared error E(N^2[n]) of the parametric grey-box linear model to fit to the initial 60sec (30sec ramp-up and 30sec steady-state tDCS) fNIRS HbT changes to tDCS, the fNIRS HbT signal without that pathway influence can be written as $Y[n] = X[n] - TF[n] * J_{tdcs}[n]$, where $TF[n]$ is the grey-box transfer function, $X[n]$ is the original fNIRS time series, and $Y[n]$ is the fNIRS time series without the corresponding pathway influence [72]. Here, initial 60sec of fNIRS HbT response was assumed to be unaffected by the cortical excitability changes since prior works showed that neuroplastic excitability after-effects (mainly calcium-dependent) start after 3 min

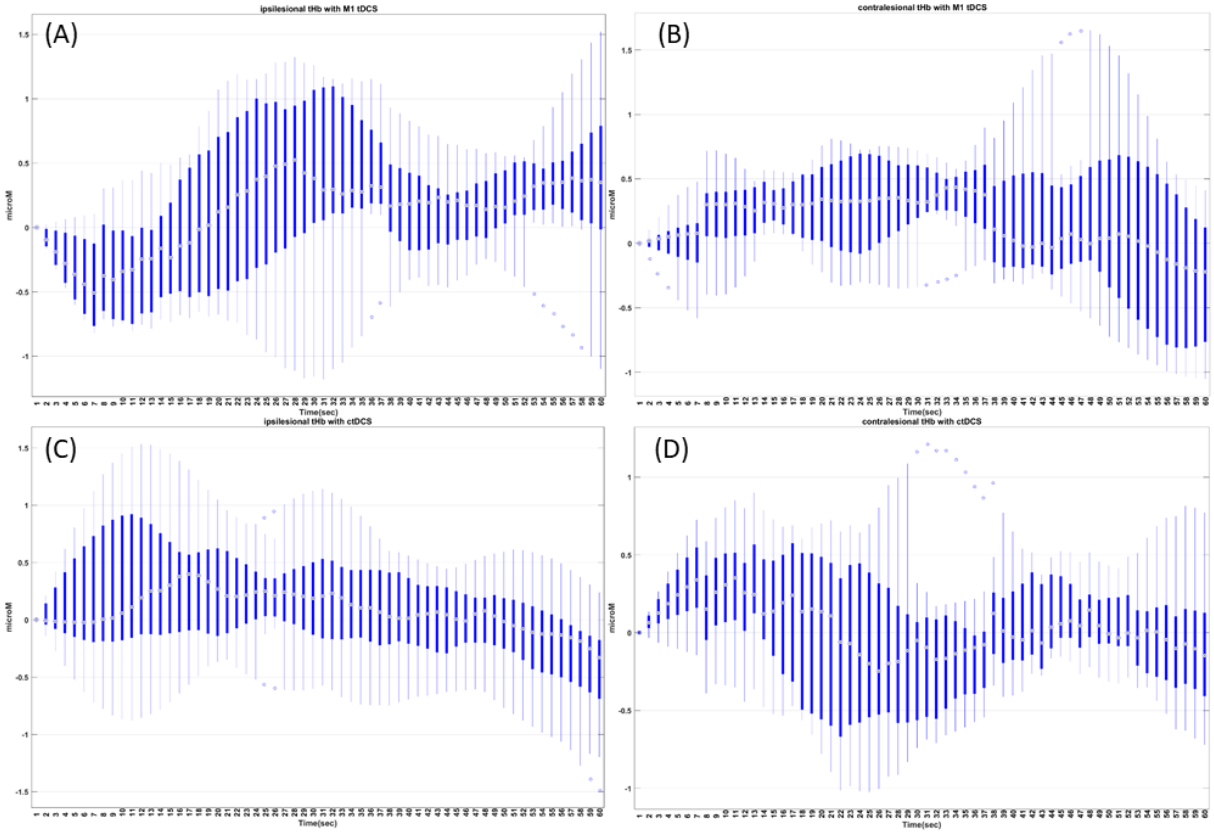

Figure 10: Box-plot of filtered HbT (microM) time-series for 0-60sec of M1 tDCS at the ipsilesional (A) and the contralesional (B) hemispheres, and for ctDCS at the ipsilesional (C) and the contralesional (D) hemispheres.

following tDCS onset [73]. We also computed the M1 tDCS and ctDCS effect size on HbT before and after removing the smooth muscle cells effects (norepinephrine [13] receptors are present on the pial arterial smooth muscle cells [14,15]). The CVR to tDCS at the ipsilesional and contralesional hemispheres were compared based on Cohen's $d = \frac{\overline{contralesional} - \overline{ipsilesional}}{\sqrt{\frac{s^3_{contralesional} - s^3_{ipsilesional}}{2}}}$, where $\overline{contralesional}$ and $\overline{ipsilesional}$ are means of the two hemisphere HbT responses, and $s_{contralesional}$ and $s_{ipsilesional}$ are their standard deviations. Paired-sample t-test was used to measure significant difference in the HbT response between the hemispheres.

Grey-box model transfer functions from physiologically detailed healthy model: The linearized grey-box model transfer functions obtained from the physiologically detailed model [31] are given in the supplementary materials: Grey-box modeling of fNIRS of tDCS effects – a chronic stroke case

Preprints (www.preprints.org) | NOT PEER-REVIEWED | Posted: 5 August 2022 doi:10.20944/preprints202208.0123.v1

series, and the model response to tDCS pulse is shown in in the supplementary materials: Grey-box modeling of fNIRS of tDCS effects – a chronic stroke case series. The response function of Pathway 1 peaked ~5 sec to the known Synaptic Potassium → vessel circumference hemodynamic responses [74]. Here, nitric oxide as postsynaptic signaling molecule is postulated to be involved later likely following facilitation of glutamate transmission with longer duration tDCS. Pathway 4 peaked ~2 sec, which can be related to cerebral autoregulation time constant [75], and can raise safety concerns vis-à-vis tDCS effects [76]. Here, the dynamic system model is postulated to be capturing the autonomic ability of cerebral arterioles to change blood volume (HbT changes) following a vasoactive tDCS stimulus [76].

Grey-box model transfer functions fitted to the post-stroke HbT – M1 tDCS data: Levenberg-Marquardt least squares search was used for iterative parameter estimation in Matlab ('tfest') to find a stable model where the regularization pulled the parameters towards the parameter values of the initial grey-box model (from the physiologically detailed healthy model [31]). Boxplot of fNIRS HbT time-series from ipsilesional and contralesional hemispheres are shown in Figure 7A and 7B with simulated results from fitted models of the four pathways shown in Figure 7C and 7D. The mean squared error (MSE) are shown in Figure 9A and 9B where Pathway 2 performed the best (lowest MSE) for ipsilesional HbT, Figure 9(A), while Pathways 1-3 performed well for contralesional HbT, Figure 9(B).

Grey-box model transfer functions fitted to the post-stroke HbT – ctDCS data: Boxplot of fNIRS HbT time-series from ipsilesional and contralesional hemispheres are shown in Figure 8A and 8B with simulated results from fitted models of the four pathways shown in Figure 8C and 8D. Iterative parameter estimation was performed for the fNIRS HbT time-series for 0-60sec of ctDCS (0-30sec ramp-up and 30-60sec steady-state) at the ipsilesional and the contralesional hemispheres. The MSE are shown in Figure 9C and 9D where Pathway 2-3 performed well for ipsilesional HbT, Figure 9(C), while Pathways 1-2 performed well for contralesional HbT, Figure 9(D).

The HbT response was significantly different (paired-sample t-test, $p<0.05$) at the ipsilesional hemisphere compared to the contralesional hemisphere in case of M1 tDCS (shown in Figure 7A and 7B) and the effect size based on Cohen's d was found to be very large (=2.49). Also, HbT response was significantly different (paired-sample t-test, $p<0.01$) at the ipsilesional hemisphere compared to the contralesional hemisphere in case of ctDCS with at a very large Cohen's d (=2.33). Then, the Pathway 4 transfer function fitted to the post-stroke HbT data (shown in Figure 7C and 7D) was used for removing Pathway 4 effects, i.e., the tDCS effects from smooth muscle cells → vessel circumference. The fNIRS HbT responses without the Pathway 4 effects are shown as box-plot in Figure 10 across all conditions: M1 tDCS, ctDCS, ipsilesional hemisphere, contralesional hemisphere. Here, the removal of Pathway 4 effects reduced Cohen's d (=0.36) and interhemispheric difference ($p=0.71$) in case of M1 tDCS. Also, the removal of the Pathway 4 effects reduced Cohen's d (=-0.266) and interhemispheric difference ($p=0.72$) in case of ctDCS.

It is postulated that the Pathway 4 effects can be via norepinephrine [13] receptors on the pial arterial smooth muscle cells [14,15] that may be relevant at the onset (<150 sec after tDCS) of tDCS [9],[31]. Also, tES-evoked LC-NE activity can have therapeutic effects, e.g., cerebellar tDCS (ctDCS) electrode [34] may stimulate the ascending fibers of the occipital nerve [77]. Here, tDCS may stimulate the peripheral nerves [33] and the LC-NE system that can also lead to psychosensory pupil response as a dilation of the pupil. Significantly, short-duration (< 3min) tDCS can have physiological effects where the biological effects can extend beyond the intended transient sensations [78]. In fact, the onset response in the case of short-duration (considered sham) tDCS may explain

Preprints (www.preprints.org) | NOT PEER-REVIEWED | Posted: 5 August 2022 doi:10.20944/preprints202208.0123.v1

the hidden source of variability in its effects [78]. In principal accordance, pupil dilation was investigated along with prefrontal fNIRS (see Figure 11a) under 2mA tDCS with anode at the FC5 and cathode at the FP2 (electrode montage from [53]) – presented next.

5 Black box modeling of prefrontal fNIRS-pupillometry of short-duration frontal tDCS effects – a healthy case series

Our prior works [6] have presented grey-box modeling results for tDCS evoked hemodynamic response; however, tDCS evoked arousal effects were not physiologically modeled explicitly [31]. In absence of grey-box model of tDCS evoked arousal effects, we tested the feasibility of black box modeling approach in this study. After informed written consent, five young (age between 20 and 30 years) and healthy male subjects were recruited. Case study procedures were performed according to the local regulations for human subjects' research at the University at Buffalo.

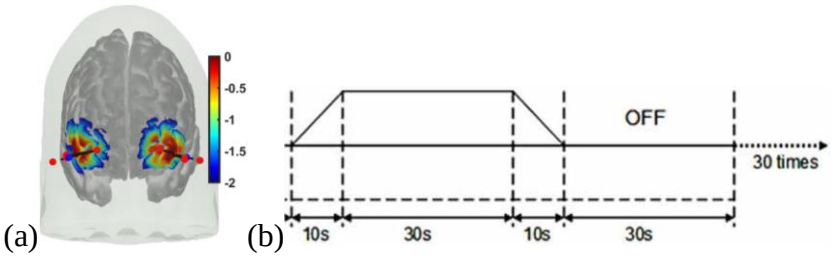

(a) (b)

Figure 11: (a) Sensitivity profile of the optode montage (red dots are sources at long separation and short separation from detectors; blue dots are detectors). The sensitivity values are displayed logarithmically with a default range of 0.01 to 1, or −2 to 0 in log10 units. (b) 30sec ON – 30sec OFF tDCS paradigm with 10sec ramp-up/10sec ramp-down – repeated 30 times in a block design.

Portable brain imaging was performed using four sources and two detectors of a portable fNIRS (Octamon+, Artinis Medical Systems, Netherlands) placed at the forehead (optode montage from [20]). Figure 11a shows the sensitivity profile of the optode montage that covered the middle frontal gyrus (orbital part) and superior frontal gyrus (dorsolateral part) bilaterally [69]. The subjects were seated comfortably indoors in a window-less room while they looked at an evenly painted non-glossy white wall with fluorescent lighting (intensity ~4000 lux). The eyes were monitored by open-source Pupil Core (Pupil Labs, Germany). Then, 2mA tDCS was applied with 30sec ON – 30sec OFF temporal sequence with 10sec ramp-up/10sec ramp-down that was repeated 30 times in a block design [62] – see Figure 11b. Stimulation and multi-modal data acquisition were synchronized using Lab Streaming Layer (https://labstreaminglayer.readthedocs.io/info/supported_devices.html).

Preprocessing of the fNIRS data was performed using standard open-source HOMER3 package (https://github.com/BUNPC/Homer3). The fNIRS preprocessing pipeline followed: first intensity was converted to optical density, and then motion artifacts were detected and filtered with the help of the Savitzky-Golay filtering method with default parameters. Then, the optical density was bandpass filtered in the neurovascular coupling band, 0.01-0.1Hz, then converted to chromophore concentration (oxyhemoglobin: HbO, deoxyhemoglobin: HHb) changes with unit partial pathlength factor. Here, vasoconstriction effects (e.g. due to tDCS-evoked norepinephrine) on the pial arteries can lead to an initial dip in the blood volume (and total hemoglobin: HbT) [31] in the long separation (LS) fNIRS channels since pial arteries start the pressure-driven blood pathway to the cortex (reviewed in Schmid et al. [45]). Also, hemodynamics in the short separation (SS) fNIRS channels can be affected by tDCS and that skin blood flow artefact need to be removed from the LS HbT data for NVU modeling. Pupil Capture (Pupil Labs, Germany) recorded the eye videos of the left and the right eyes at 120 fps in 400x400 pixel resolution. Pupil Core reports pupil diameter in ‘mm’ provided

Preprints (www.preprints.org) | NOT PEER-REVIEWED | Posted: 5 August 2022 doi:10.20944/preprints202208.0123.v1

by the pye3d model [79]. The timeseries from the left and the right eye were averaged in the young and healthy subjects.

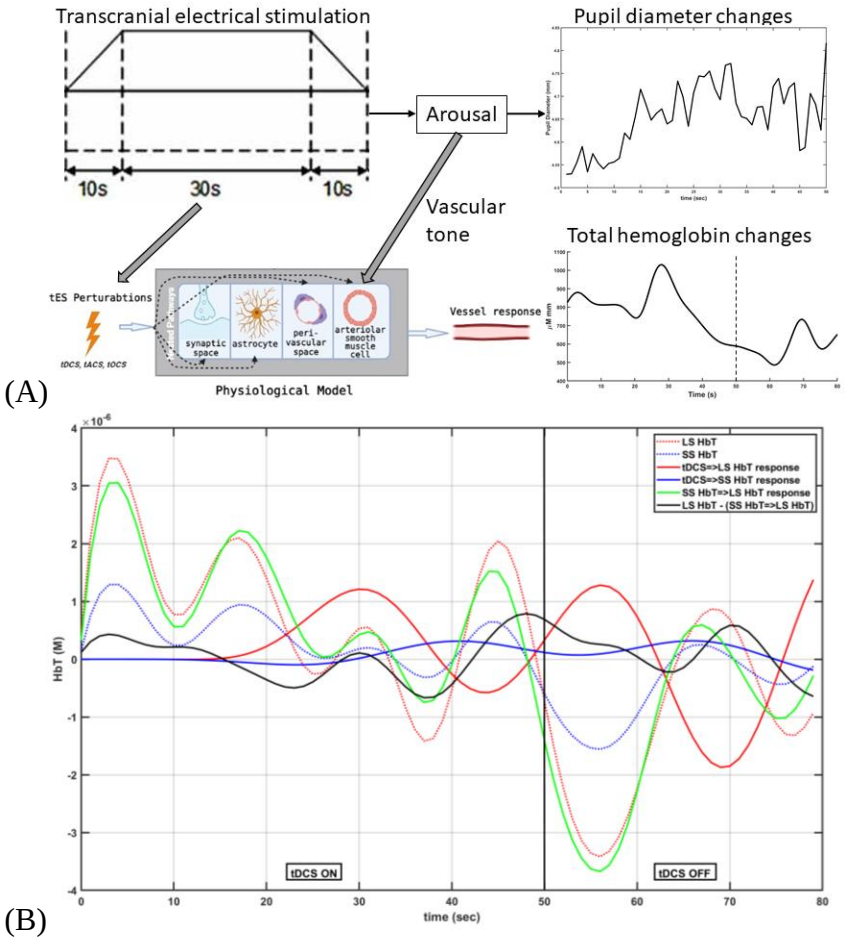

Figure 12: (A) Transcranial electrical stimulation evoked arousal leads to changes in the pupil diameter as well as the vascular tone that affects the evoked hemodynamic response. (B) An illustrative example of HbT responses in long separation (LS) and short separation (SS) fNIRS channels. LS HbT: long separation total hemoglobin changes, SS HbT: short separation total hemoglobin changes, tDCS=>LS HbT response: transfer function response with tDCS waveform input and LS HbT output, tDCS=>SS HbT response: transfer function response with tDCS waveform input and SS HbT output, SS HbT=>LS HbT response: transfer function response with SS HbT input and LS HbT output, LS HbT-(SS HbT=>LS HbT): SS HbT=>LS HbT response subtracted from LS HbT.

Figure 12A shows the postulated relation between the pupil diameter changes and the total hemoglobin concentration changes (HbT=HbO+HHb) due to tDCS evoked arousal. A state-space model for arousal via reduction of a regularized ARX model ('ssregest' in Matlab) was found between the tDCS trapezoidal waveform input and the pupil diameter changes output [80] that could account for the carry-over effect. Also, transfer functions were estimated ('tfest' with EnforceStability estimation option as true in Matlab) for LS HbT and SS HbT responses and the estimated model responses ('lsim' in Matlab) for the tDCS ON-OFF period are shown in Figure 12B. Figure 12B shows an illustrative example of averaged LS HbT and averaged SS HbT signals across tDCS ON-OFF period (total 80 sec). The model from tDCS waveform input to LS HbT output (tDCS=>LS in Figure 12B) was initialized with reduced-dimension model (8 poles, 2 zeros [31]) for Pathway 3: Perivascular Potassium → vessel circumference. The model from tDCS waveform input to SS HbT output (tDCS=>SS in Figure 12B) was initialized with reduced-dimension model (6 poles, 1 zeros [31]) for Pathway 4: Smooth muscle cell → vessel circumference. The model from SS HbT input to LS HbT output (SS=>LS in Figure 12B) was a static gain model. All the transfer functions are presented in the supplementary materials: Black box modeling of prefrontal fNIRS-pupillometry of short-duration frontal tDCS effects – a healthy case series.

Preprints (www.preprints.org) | NOT PEER-REVIEWED | Posted: 5 August 2022 doi:10.20944/preprints202208.0123.v1

The transfer function from SS HbT input to LS HbT output provided the estimation of the skin blood flow artefact that was removed from the LS HbT signal. Then, the transfer function between the tDCS trapezoidal waveform input and the skin-artefact-free LS fNIRS HbT output was computed. The state-space model via reduction of a regularized ARX model between the pupil diameter changes input and the skin-artefact-free LS fNIRS HbT output provided insights. For example, an anti-correlation relationship between tDCS evoked pupil diameter changes (pupil dilation) and the blood volume changes (HbT) was found. The impulse response ('impulseplot' in Matlab) and power spectrum ('spectrum' in Matlab) of all the state-space models of each subject are presented in the supplementary materials: Black box modeling of prefrontal fNIRS-pupillometry of short-duration frontal tDCS effects – a healthy case series. Then, the step-response characteristics ('stepinfo' in Matlab) for the dynamic system model between the tDCS trapezoidal waveform input and the prefrontal average HbT changes (across all fNIRS channels) output is shown in Table 1a, between the tDCS trapezoidal waveform input and the pupil diameter changes output is shown in Table 1b, and between the pupil diameter changes input and the average HbT changes (across all fNIRS channels) output is shown in Table 1c. Here, the rise time, i.e., the time it takes for the response to go from 10% to 90%, was fastest (2.54±0.44sec) for the model between the tDCS trapezoidal waveform input and the prefrontal average HbT changes output (Table 1a), followed by the dynamic system model between the tDCS trapezoidal waveform input and the pupil diameter changes output (7.16±5.01sec) and the dynamic system model between the pupil diameter changes input and the average HbT changes output (10.02±3.01sec). Therefore, it can be postulated that tDCS evoked hemodynamic response has an immediate onset that is faster than the effect via arousal pathways. The immediate onset has the fastest rise time (2.54±0.44sec), i.e., ~2 sec comparable to the cerebral autoregulation time constant [75], for the dynamic system model between the tDCS trapezoidal waveform input and the prefrontal average HbT changes output.

Table 1a: Step-response characteristics for dynamic system model between the tDCS trapezoidal waveform input and the prefrontal average HbT changes (across all fNIRS channels) output - tDCS2HbT

tDCS2HbT	Subject 1	Subject 2	Subject 3	Subject 4	Subject 5	mean	stdev
RiseTime	2.4	2.3	2.2	2.5	3.3	2.54	0.439318
SettlingTime	9.6	8.7	9.9	10.4	9.4	9.6	0.62849
SettlingMin	0.2187	0.2544	0.2882	0.1615	0.1351	0.21158	0.063467
SettlingMax	0.5878	0.6019	0.5944	0.587	0.5628	0.58678	0.014687
Overshoot	0.7288	12.9567	7.6098	0.118	0.2432	4.3313	5.757355
Undershoot	0	0	0	0	0	0	0
Peak	0.5878	0.6019	0.5944	0.587	0.5628	0.58678	0.014687
PeakTime	4	4.6	4.1	14.6	14.2	8.3	5.574944

Table 1b: Step-response characteristics for dynamic system model between the tDCS trapezoidal waveform input and the pupil diameter changes output - tDCS2PD

tDCS2PD	Subject 1	Subject 2	Subject 3	Subject 4	Subject 5	mean	stdev
RiseTime	14.2	3.5	8.3	8.5	1.3	7.16	5.00979
SettlingTime	16.1	11.3	19.2	12	13.9	14.5	3.221025
SettlingMin	0.6813	0.5992	0.7907	0.6583	0.2203	0.58996	0.21797
SettlingMax	0.7559	0.665	0.8782	0.7285	0.7287	0.75126	0.078427
Overshoot	0	0.665	0	0	0.1329	0.15958	0.288339
Undershoot	225.1942	127.3642	14.2983	0	0	73.37134	100.2768
Peak	1.7037	0.8472	0.8782	0.7285	0.7287	0.97726	0.411736

Preprints (www.preprints.org) | NOT PEER-REVIEWED | Posted: 5 August 2022 doi:10.20944/preprints202208.0123.v1

PeakTime	4.5	4.2	53.9	18.6	20.7	20.38	20.25357

Table 1c: Step-response characteristics for dynamic system model between the pupil diameter changes input and the average HbT changes (across all fNIRS channels) output – PD2HbT

PD2HbT	Subject 1	Subject 2	Subject 3	Subject 4	Subject 5	mean	stdev
RiseTime	11.7	7.5	6.5	10.6	13.8	10.02	3.007823
SettlingTime	20.6	14.1	11	19.3	25.8	18.16	5.77434
SettlingMin	0.6935	0.738	0.568	0.7148	0.6868	0.68022	0.065855
SettlingMax	0.769	0.819	0.629	0.7922	0.762	0.75424	0.073481
Overshoot	0	0	0	0	0	0	0
Undershoot	0.5904	0.4861	0	4.4144	0	1.09818	1.873619
Peak	0.769	0.819	0.629	0.7922	0.762	0.75424	0.073481
PeakTime	33.9	25.6	17.9	50.7	47.9	35.2	14.09503

Granger causality and block exogeneity tests for vector autoregression (VAR) models were conducted using Matlab (The Mathworks, Inc., USA) to check if tDCS waveform was block exogenous, i.e., if tDCS waveform do not Granger-cause pupil diameter changes (pupil dilation) and blood volume changes (HbT) in the multivariate system. First, the time series analysis of the tDCS evoked pupil diameter changes (pupil dilation) and blood volume changes (HbT) showed that the autocorrelation function decreased slowly while the partial autocorrelation function converged to zero after about 8 lags. An augmented Dickey-Fuller test ('adftest' in Matlab) confirmed that all signals were stationary ($p < 0.025$). The innovation errors were investigated for normality ($p < 0.025$) and the remaining autocorrelation structure of the innovation error was found to be negligible. Then, VAR model for the tDCS waveform, HbT timeseries and pupil dilation timeseries was fitted, and the block exogeneity test rejected the claim that the tDCS waveform is not a 1-step Granger-cause of the HbT timeseries and pupil dilation timeseries ($p<0.05$). The results of the VAR model analysis are presented for each subject in the supplementary materials: Black box modeling of prefrontal fNIRS-pupillometry of short-duration frontal tDCS effects – a healthy case series.

It is postulated that VAR models may be leveraged for immediate control of hemodynamics using model predictive control (MPC). MPC uses an internal model for making predictions of the system behavior, considering the dynamics over a predefined prediction horizon, for optimizing the control actions. For online operation, MPC operates in a receding horizon fashion, i.e., new system measurements and new predictions into the future are made at each time step. Here, MPC can be based on a minimal realization transfer functions for the four nested pathways for NVU [31], where tES current density (input) can perturb a state variable at each of the four NVU compartments to perturb the vessel volume response (output).

6 Human-in-the-loop optimization for model predictive control of tES evoked HbT

Yashika et al. [46] found that the vessel oscillations were more sensitive to transcranial oscillating current stimulation (tOCS) than to the transcranial alternating current stimulation (tACS), and the effects were more pronounced for lower frequencies within the frequency range of 0.1 Hz to 10 Hz. Here, increases in interstitial potassium concentration can modulate the neurovascular coupling [31], i.e., the Pathway 3: tES perturbing vessel response through perivascular potassium pathway. Then, a change in the transfer function model from tDCS waveform (input) to the HbT response (output) can change the steady state gain of the system which is postulated via the Kir channels [49]. Therefore, in a healthy case study, we aimed to test the feasibility of human-in-the-

Preprints (www.preprints.org) | NOT PEER-REVIEWED | Posted: 5 August 2022 doi:10.20944/preprints202208.0123.v1

loop optimization of tOCS and tACS with the electrodes placed at the 'FT7' and 'FT8' EEG locations (10-10 system) to maximize the steady state gain (i.e., moles of HbT change per mA of tES current intensity) of the Pathway 3 (reduced dimension model [31]) that was fitted ('tfest' with EnforceStability estimation option as true in Matlab) to the tES evoked skin-artefact-free LS HbT data from frontal fNIRS optodes (Sensitivity profile shown in Figure 11A). The electric field computed with the ROAST package [57] are presented in the supplementary materials: Human-in-the-loop optimization for model predictive control of tES evoked HbT. The model predictive control scheme is shown in Figure 13 where the skin-artefact-free LS HbT response was used to optimize tOCS control actions, i.e., the tES waveform was parametrized by a direct current (DC) intensity, an alternating current (AC) amplitude, and AC frequency. The amplitude of the AC waveform had a fixed ramp-up time (=10 sec), ramp-down time (=10 sec), and duration (=10 sec). Repeated measures of the 30sec epochs of tOCS evoked skin-artefact-free LS HbT response was used by the CMA-ES algorithm [47] to optimize the DC intensity, AC amplitude, and AC frequency for the following iteration of the 30sec tOCS ON period to maximize the steady state gain of the system (i.e., Pathway 3 model fitted to tOCS ON HbT data). Here, the mean of the set of current intensity perturbations at each iteration, which is evaluated independently, is the optimal current intensity at that stage of the optimization.

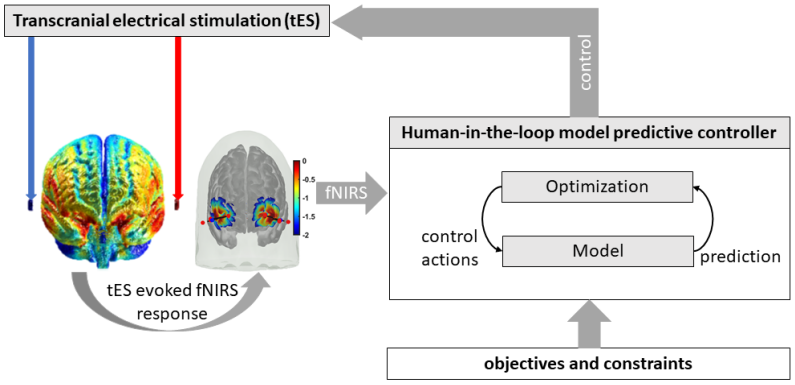

Figure 13: An illustrative model predictive control scheme.

 doi:10.20944/preprints202208.0123.v1

A case study (male, 44 years old) study was performed after informed written consent according to the local regulations for human subjects' research. Case report procedures were performed according to the local regulations for human subjects' research at the University at Buffalo. Portable brain imaging was performed using four sources and two detectors of a portable fNIRS (Octamon+, Artinis Medical Systems, Netherlands) placed at the forehead (optode montage from [20]). Figure 11a shows the sensitivity profile of the optode montage that covered the middle frontal gyrus (orbital part) and superior frontal gyrus (dorsolateral part) bilaterally [69]. Stimulation and multi-modal data acquisition were synchronized using Lab Streaming Layer

 doi:10.20944/preprints202208.0123.v1

(https://labstreaminglayer.readthedocs.io/info/supported_devices.html). Online preprocessing of the

Preprints (www.preprints.org) | NOT PEER-REVIEWED | Posted: 5 August 2022 doi:10.20944/preprints202208.0123.v1

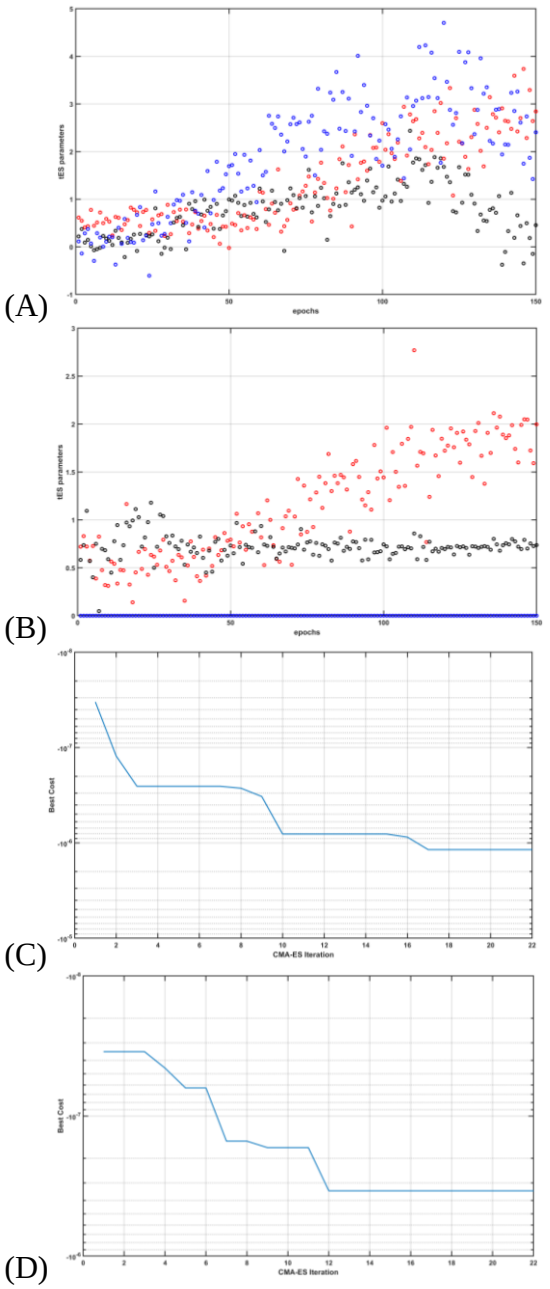

Figure 14: Human-in-the-loop optimization using Covariance Matrix Adaptation Evolution Strategy (CMA-ES). (A) tOCS parameters: DC intensity in mA (blue), AC amplitude in mA (red), and AC frequency in Hz (black). (B) tACS parameters: DC intensity = 0 mA (blue), AC amplitude in mA (red), and AC frequency in Hz (black). (C) Best cost (=negative steady state gain of HbT in M) for tOCS over 22 iterations of CMA-ES. (D) Best cost (HbT in M) for tACS over 22 iterations of CMA-ES.

30sec fNIRS data epoch after the end of the tOCS ON period was performed in Matlab using functions from the open-source HOMER3 package (https://github.com/BUNPC/Homer3). The fNIRS preprocessing pipeline followed: first intensity was converted to optical density, and then motion artifacts were detected and filtered with the help of the Savitzky-Golay filtering method with default parameters. Then, the optical density was bandpass filtered in the neurovascular coupling band, 0.01-0.1Hz, then converted to chromophore concentration (oxyhemoglobin: HbO, deoxyhemoglobin: HHb) changes with unit partial pathlength factor. We averaged all the long separation (LS) HbT channels and all the short separation (SS) HbT channels for online model estimation following the 30sec tDCS ON perturbation using MatNIC2 is a Matlab toolkit (Neuroelectrics, USA). First, the static gain transfer function from SS HbT input to LS HbT output provided the estimation of the skin blood flow artefact during tOCS ON epoch that was removed from the LS HbT signal. Then, the steady state gain ('dcgain' in Matlab) of the Pathway 3 fitted ('tfest' with EnforceStability estimation option as true in Matlab) to the 30 sec epoch of the tOCS evoked skin-artefact-free LS HbT data was estimated. Then, the CMA-ES algorithm [47] computed the DC intensity, AC amplitude, and AC frequency for the next perturbation and the iterations continued for 150 epochs as shown in the Figure 14A. Figure 14B shows the case where the DC intensity was set to zero and only the AC amplitude, and the AC frequency were optimized (i.e., tACS condition). CMA-ES took 7 epochs of tES perturbation to deliver one iteration of optimization. The change in the best cost (i.e., the negative of steady state gain, HbT in microM) from 7 epochs for each iteration of the CMA-ES optimization in Figure 14C and 14D for tOCS and tACS respectively. Here, tOCS reached a higher steady state gain for the Pathway 3 than tACS over 22 CMA-ES iterations (took ~75 mins) that aligned with our computational modeling results [46]; however, optimal tOCS parameters likely require more epochs of human-in-the-loop optimization when compared to lesser parameters for tACS. Notably, optimal frequency settled around >0.5 Hz for tACS that aligned well with the stable modes (see Figure 4) near 1 Hz for the tES Pathway 3. Future work needs to test the feasibility of human-

Preprints (www.preprints.org) | NOT PEER-REVIEWED | Posted: 5 August 2022 doi:10.20944/preprints202208.0123.v1

in-the-loop optimization for model predictive control of other pathways including tES evoked oxidative metabolic substrates that can provide therapeutic intervention in mild cognitive impairment and T2DM. However, such human-in-the-loop optimization of metabolic state will require development of computational model to estimate the metabolic state of the tissue in the future.

7 Discussion

Our computational review focused on systems analysis using published physiologically detailed grey-box model [31] and black box model [8] that provided insights into tDCS evoked responses in fMRI data, fNIRS data, and pupillometry data. We also showed a single subject feasibility of human-in-the-loop optimization for model predictive control of tES evoked HbT with a case study. Notably, the AC frequency was found to settle around 1 Hz (~0.8 Hz for tACS) after 22 CMA-ES iterations while the AC amplitude reached around 2mA in the tACS condition (see Figure 14B). This “optimal” AC frequency value from CMA-ES aligned well with the results from modal analysis of the tES pathways (see Figure 4) where stable modes were found near 1 Hz, especially for the Pathways 2 and 3, which needs mechanistic (vis-à-vis astrocytes, interstitial potassium) investigation using animal models [81],[82]. Then, the relationship between fNIRS and pupillometry data needs further investigation vis-à-vis arousal mechanisms. Arousal mechanisms has broad implications on the bedside neuromonitoring of disorders of consciousness [83], including Alzheimer's disease [84], where monitoring of the neurovascular coupling [3] and pupil dilation [1],[2] may be feasible. For bedside neuromonitoring, an important aspect is the neurometabolic state of the brain that is partly regulated by tonic and phasic norepinephrine activity [85]. In this computational review paper, we showed that tDCS-evoked hemodynamic response and pupil dilation can be related in healthy individuals, postulated to be subserved by arousal mechanisms, where future studies need to investigate this relationship in disorders of consciousness including Alzheimer's disease. Moreover, subject-specific interaction [86] between the tDCS-evoked LC-NE activity and the postulated increase in the interstitial potassium concentration, which can modulate neurovascular coupling [31], can provide insights into the inter-individual variability in tES effects [6]. Then, tES-evoked increase in energy demand can uncover abnormalities [7] of cerebral metabolism that can be elucidated with system analysis of the neuroimaging data. For example, a decreased availability of oxidative metabolic substrates in the NE-depleted cortex can be partly responsible for mild cognitive impairment and “brain fog” [87],[88]. Then, human-in-the-loop optimization for model predictive control of tES evoked LC-NE activity (measured with pupil dilation) and metabolic substrates can provide therapeutic intervention in mild cognitive impairment and T2DM.

Increase in CBF and oxy-hemoglobin concentration during tES need careful investigation to delineate two main neurovascular coupling hypotheses – a metabolic and neurogenic. Indirect "metabolic hypothesis" states that an increase in neuronal synaptic activity causes additional energy and oxygen demand, causing various vasodilation agents to send signals to cerebral vasculature for vasodilation, resulting in an increase in CBF and oxy-hemoglobin. Increase in oxy-hemoglobin can also be explained through direct "neurogenic hypothesis," whereby the direct electric field modulation of neuropeptides and neurotransmitters causes a discharge of various vasoactive agents for vasodilation. So, "neurogenic hypothesis" can also be applied to the tDCS effects on the perivascular nerves, e.g., in the pial vasculature, which will have a compounding effect to change oxy-hemoglobin levels. Therefore, early and late hemodynamic response to plasticity-inducing tDCS need to be carefully investigated in the future works where “metabolic hypothesis" vis-à-vis cortical excitability alterations (polarity dependent M1 tDCS effect [73]) need to be delineated from "neurogenic hypothesis" vis-à-vis tDCS effects on the perivascular nerves. Here, complex

 doi:10.20944/preprints202208.0123.v1

bidirectional interactions can lead to non-linear dose-effect [89] where lower current intensity at the scalp will primarily affect the perivascular nerves in the pial vasculature while higher current intensity at the scalp may reach deeper in the cortex – a dose-response effect.

Future works need to investigate human-in-the-loop optimization for model predictive control of non-invasive brain stimulation to address cognitive impairments in T2DM and early stage AD that can be based on the Hemo-Neural Hypothesis [51]. Animal studies provided some insights into the application of tES, e.g., a study by Han et al. [90] found that the concentration of oxyhemoglobin increased almost linearly during tDCS and then decreased linearly immediately after the termination of tDCS with a similar rate of change that differed from rat to rat. Han et al. [90] suggested that individual differences in anodal tDCS's neuronal aftereffects may be related to individual variability in the rate of change of hemodynamic response to tDCS. In Han et al. study [90], the concentration of deoxygenated hemoglobin did not show a significant difference during and after tDCS [90]. Here, direct effects of tDCS on cortical astrocytes with astrocyte regulation of blood flow [91] is possible that can be without changes in the local field potential [92] which can also lead to dilation or constriction of the arterioles [93]. Wachter et al. [94] showed sustained polarity-specific changes in CBF using laser Doppler blood perfusion imaging (LDI), where the duration and the degree of CBF changes depended on the intensity of the current applied. Moreover, Mielke et al. [95], using LDI, showed regionally limited, long-lasting, and reversible decrease in hemispheric CBF due to cathodal tDCS that depended on the current intensity as well as the size of the stimulation electrode. Also, patient-derived cerebral organoids can facilitate individualizing non-invasive brain stimulation applications, including photobiomodulation [96], to address state-trait differences [97]. Here, patient-derived cerebral organoids can reveal trait-differences and gene expression patterns subserving dysregulation of mitochondrial function [98] and metabolic state. For example, “phase zero” cerebral organoid platform [96] can use dual polymer sensor in the Matrigel matrix to provide real-time monitoring of glucose and oxygen [99] during stimulation to capture dose/response relationship with systems analysis. Then, organoid-in-the-loop optimization for model predictive control of non-invasive stimulation can be individualized and tested for feasibility before conducting resource intensive human clincal studies. Future invasive animal studies need to investigate the plasticity of the modulation of the mural cells [100] by long-term tES for the mechanistic understanding of the tES effects on neurovascular and neurometabolic coupling.

Limitation of the current work includes unavailability of the fMRI-EEG data to demonstrate the long-term effects of tES on the neurovascular coupling, where fNIRS-EEG has been shown feasible by computational modeling [8],[9]. Also, the trade-off between bias (in canonical HRF) and variance (in FIR HRF) that can be achieved by applying mechanistic grey-box modeling of the NVU pathways was not demonstrated in this current study.

8 Conflict of Interest

The authors declare that the research was conducted in the absence of any commercial or financial relationships that could be construed as a potential conflict of interest.

9 Author Contributions

Yashika Arora

ROLES: Data curation, Formal analysis, Investigation, Methodology, Software, Validation, Visualization, Writing – original draft.

Anirban Dutta

ROLES: Conceptualization, Formal analysis, Investigation, Methodology, Project administration, Resources, Supervision, Validation, Visualization, Writing – original draft, review & editing.

10 Funding

The computational research was conducted at the Neuroengineering and Informatics for Rehabilitation Laboratory, University at Buffalo, and was funded by the Community for Global Health Equity at the University at Buffalo, USA (Anirban Dutta) and the fellowship (Yashika Arora) from Science and Engineering Research Board, a statutory body of the Department of Science and Technology, Government of India, and Ministry of Electronics and Information Technology, Government of India. The funders had no role in study design, data collection and analysis, decision to publish, or preparation of the manuscript.

11 Acknowledgments

Authors would like to acknowledge the retrospective data from the stroke study at the All India Institute of Medical Sciences, New Delhi, India that was funded by the Indian Department of Health Research, Project Code No. N1761. The retrospective data from human studies, in collaboration with Dr. Uttama Lahiri at Indian Institute of Technology Gandhinagar, was funded by the Indian Ministry of Human Resource Development (MHRD)′s Scheme for Promotion of Academic and Research Collaboration (SPARC), grant number 2018−2019/P721/SL.

12 Reference

1. Vassilieva, A.; Olsen, M.H.; Peinkhofer, C.; Knudsen, G.M.; Kondziella, D. Automated Pupillometry to Detect Command Following in Neurological Patients: A Proof-of-Concept Study. *PeerJ* **2019**, *7*, e6929, doi:10.7717/peerj.6929.
2. Olsen, M.H.; Jensen, H.R.; Ebdrup, S.R.; Topp, N.H.; Strange, D.G.; Møller, K.; Kondziella, D. Automated Pupillometry and the FOUR Score — What Is the Diagnostic Benefit in Neurointensive Care? *Acta Neurochir* **2020**, *162*, 1639–1645, doi:10.1007/s00701-020-04381-y.
3. Othman, M.H.; Bhattacharya, M.; Møller, K.; Kjeldsen, S.; Grand, J.; Kjaergaard, J.; Dutta, A.; Kondziella, D. Resting-State NIRS-EEG in Unresponsive Patients with Acute Brain Injury: A Proof-of-Concept Study. *Neurocrit Care* **2020**, doi:10.1007/s12028-020-00971-x.
4. Chougule, P.S.; Najjar, R.P.; Finkelstein, M.T.; Kandiah, N.; Milea, D. Light-Induced Pupillary Responses in Alzheimer's Disease. *Front Neurol* **2019**, *10*, 360, doi:10.3389/fneur.2019.00360.
5. Chan, L.; Liao, Y.-C.; Mo, G.B.; Dudley, J.J.; Cheng, C.-L.; Kristensson, P.O.; Oulasvirta, A. Investigating Positive and Negative Qualities of Human-in-the-Loop Optimization for Designing Interaction Techniques. In Proceedings of the Proceedings of the 2022 CHI Conference on Human Factors in Computing Systems; Association for Computing Machinery: New York, NY, USA, April 27 2022; pp. 1–14.
6. Dutta, A. Simultaneous Functional Near-Infrared Spectroscopy (FNIRS) and Electroencephalogram (EEG) to Elucidate Neurovascular Modulation by Transcranial

Electrical Stimulation (TES). *Brain Stimul* **2021**, *14*, 1093–1094, doi:10.1016/j.brs.2021.07.019.

7. Dutta, A.; Jacob, A.; Chowdhury, S.R.; Das, A.; Nitsche, M.A. EEG-NIRS Based Assessment of Neurovascular Coupling during Anodal Transcranial Direct Current Stimulation--a Stroke Case Series. *J Med Syst* **2015**, *39*, 205, doi:10.1007/s10916-015-0205-7.
8. Sood, M.; Besson, P.; Muthalib, M.; Jindal, U.; Perrey, S.; Dutta, A.; Hayashibe, M. NIRS-EEG Joint Imaging during Transcranial Direct Current Stimulation: Online Parameter Estimation with an Autoregressive Model. *J. Neurosci. Methods* **2016**, *274*, 71–80, doi:10.1016/j.jneumeth.2016.09.008.
9. Arora, Y.; Walia, P.; Hayashibe, M.; Muthalib, M.; Chowdhury, S.R.; Perrey, S.; Dutta, A. Grey-Box Modeling and Hypothesis Testing of Functional near-Infrared Spectroscopy-Based Cerebrovascular Reactivity to Anodal High-Definition TDCS in Healthy Humans 2021.
10. Guhathakurta, D.; Dutta, A. Computational Pipeline for NIRS-EEG Joint Imaging of TDCS-Evoked Cerebral Responses—An Application in Ischemic Stroke. *Front. Neurosci.* **2016**, *10*, doi:10.3389/fnins.2016.00261.
11. Schmid, P.J. Dynamic Mode Decomposition and Its Variants. *Annual Review of Fluid Mechanics* **2022**, *54*, 225–254, doi:10.1146/annurev-fluid-030121-015835.
12. Stefanovska, A.; Bracic, M.; Kvernmo, H.D. Wavelet Analysis of Oscillations in the Peripheral Blood Circulation Measured by Laser Doppler Technique. *IEEE Trans Biomed Eng* **1999**, *46*, 1230–1239, doi:10.1109/10.790500.
13. Mishima, T.; Nagai, T.; Yahagi, K.; Akther, S.; Oe, Y.; Monai, H.; Kohsaka, S.; Hirase, H. Transcranial Direct Current Stimulation (TDCS) Induces Adrenergic Receptor-Dependent Microglial Morphological Changes in Mice. *eNeuro* **2019**, *6*, doi:10.1523/ENEURO.0204-19.2019.
14. Wahl, M.; Kuschinsky, W.; Bosse, O.; Olesen, J.; Lassen, N.A.; Ingvar, D.H.; Michaelis, J.; Thurau, K. Effect of I-Norepinephrine on the Diameter of Pial Arterioles and Arteries in the Cat. *Circulation Research* **1972**, *31*, 248–256, doi:10.1161/01.RES.31.2.248.
15. Liu, Y.; Yang, X.; Gong, H.; Jiang, B.; Wang, H.; Xu, G.; Deng, Y. Assessing the Effects of Norepinephrine on Single Cerebral Microvessels Using Optical-Resolution Photoacoustic Microscope. *JBO* **2013**, *18*, 076007, doi:10.1117/1.JBO.18.7.076007.
16. Fonseca, D.A.; Antunes, P.E.; Antunes, M.J.; Cotrim, M.D. Vasomotion as an Oscillatory Sign of Functional Impairment in the Human Internal Thoracic Artery: A Study Based on Risk Factors and Vessel Reactivity. *Exp Physiol* **2018**, *103*, 1030–1038, doi:10.1113/EP087002.
17. Sharp, M.K.; Diem, A.K.; Weller, R.O.; Carare, R.O. Peristalsis with Oscillating Flow Resistance: A Mechanism for Periarterial Clearance of Amyloid Beta from the Brain. *Ann Biomed Eng* **2016**, *44*, 1553–1565, doi:10.1007/s10439-015-1457-6.
18. Hladky, S.B.; Barrand, M.A. Elimination of Substances from the Brain Parenchyma: Efflux via Perivascular Pathways and via the Blood–Brain Barrier. *Fluids and Barriers of the CNS* **2018**, *15*, 30, doi:10.1186/s12987-018-0113-6.
19. Geddes, J.B.; Carr, R.T.; Wu, F.; Lao, Y.; Maher, M. Blood Flow in Microvascular Networks: A Study in Nonlinear Biology. *Chaos* **2010**, *20*, 045123, doi:10.1063/1.3530122.

20. Zhao, F.; Tomita, M.; Dutta, A. Functional Near-Infrared Spectroscopy Of Prefrontal Cortex During Memory Encoding And Recall In Elderly With Type 2 Diabetes Mellitus. **2022**, doi:10.20944/preprints202202.0045.v1.

21. Kisler, K.; Nelson, A.R.; Montagne, A.; Zlokovic, B.V. Cerebral Blood Flow Regulation and Neurovascular Dysfunction in Alzheimer Disease. *Nat Rev Neurosci* **2017**, *18*, 419–434, doi:10.1038/nrn.2017.48.

22. Pan, Y.; Li, H.; Wardlaw, J.M.; Wang, Y. A New Dawn of Preventing Dementia by Preventing Cerebrovascular Diseases. *BMJ* **2020**, *371*, m3692, doi:10.1136/bmj.m3692.

23. Zheng, X.; Alsop, D.C.; Schlaug, G. Effects of Transcranial Direct Current Stimulation (TDCS) on Human Regional Cerebral Blood Flow. *Neuroimage* **2011**, *58*, 26–33, doi:10.1016/j.neuroimage.2011.06.018.

24. Jindal, U.; Sood, M.; Dutta, A.; Chowdhury, S.R. Development of Point of Care Testing Device for Neurovascular Coupling From Simultaneous Recording of EEG and NIRS During Anodal Transcranial Direct Current Stimulation. *IEEE Journal of Translational Engineering in Health and Medicine* **2015**, *3*, 1–12, doi:10.1109/JTEHM.2015.2389230.

25. Mijajlović, M.D.; Pavlović, A.; Brainin, M.; Heiss, W.-D.; Quinn, T.J.; Ihle-Hansen, H.B.; Hermann, D.M.; Assayag, E.B.; Richard, E.; Thiel, A.; et al. Post-Stroke Dementia – a Comprehensive Review. *BMC Medicine* **2017**, *15*, 11, doi:10.1186/s12916-017-0779-7.

26. Shabir, O.; Berwick, J.; Francis, S.E. Neurovascular Dysfunction in Vascular Dementia, Alzheimer's and Atherosclerosis. *BMC Neuroscience* **2018**, *19*, 62, doi:10.1186/s12868-018-0465-5.

27. Binkofski, F.; Loebig, M.; Jauch-Chara, K.; Bergmann, S.; Melchert, U.H.; Scholand-Engler, H.G.; Schweiger, U.; Pellerin, L.; Oltmanns, K.M. Brain Energy Consumption Induced by Electrical Stimulation Promotes Systemic Glucose Uptake. *Biol Psychiatry* **2011**, *70*, 690–695, doi:10.1016/j.biopsych.2011.05.009.

28. Scholey, A.B.; Harper, S.; Kennedy, D.O. Cognitive Demand and Blood Glucose. *Physiol Behav* **2001**, *73*, 585–592, doi:10.1016/s0031-9384(01)00476-0.

29. Dienel, G.A.; Cruz, N.F. Aerobic Glycolysis during Brain Activation: Adrenergic Regulation and Influence of Norepinephrine on Astrocytic Metabolism. *Journal of Neurochemistry* **2016**, *138*, 14–52, doi:10.1111/jnc.13630.

30. Bekar, L.K.; Wei, H.S.; Nedergaard, M. The Locus Coeruleus-Norepinephrine Network Optimizes Coupling of Cerebral Blood Volume with Oxygen Demand. *J Cereb Blood Flow Metab* **2012**, *32*, 2135–2145, doi:10.1038/jcbfm.2012.115.

31. Arora, Y.; Walia, P.; Hayashibe, M.; Muthalib, M.; Chowdhury, S.R.; Perrey, S.; Dutta, A. Grey-Box Modeling and Hypothesis Testing of Functional near-Infrared Spectroscopy-Based Cerebrovascular Reactivity to Anodal High-Definition TDCS in Healthy Humans. *PLOS Computational Biology* **2021**, *17*, e1009386, doi:10.1371/journal.pcbi.1009386.

32. Montefusco-Siegmund, R.; Schwalm, M.; Jubal, E.R.; Devia, C.; Egaña, J.I.; Maldonado, P.E. Alpha EEG Activity and Pupil Diameter Coupling during Inactive Wakefulness in Humans. *eNeuro* **2022**, *9*, doi:10.1523/ENEURO.0060-21.2022.

33. Vanneste, S.; Mohan, A.; Yoo, H.B.; Huang, Y.; Luckey, A.M.; McLeod, S.L.; Tabet, M.N.; Souza, R.R.; McIntyre, C.K.; Chapman, S.; et al. The Peripheral Effect of Direct Current

Stimulation on Brain Circuits Involving Memory. *Science Advances* **2020**, *6*, eaax9538, doi:10.1126/sciadv.aax9538.

34. Rezaee, Z.; Ranjan, S.; Solanki, D.; Bhattacharya, M.; Srivastava, M.V.P.; Lahiri, U.; Dutta, A. Feasibility of Combining Functional Near-Infrared Spectroscopy with Electroencephalography to Identify Chronic Stroke Responders to Cerebellar Transcranial Direct Current Stimulation-a Computational Modeling and Portable Neuroimaging Methodological Study. *Cerebellum* **2021**, doi:10.1007/s12311-021-01249-4.

35. Larsen, R.S.; Waters, J. Neuromodulatory Correlates of Pupil Dilation. *Frontiers in Neural Circuits* **2018**, *12*.

36. Diehl, R.R.; Linden, D.; Lücke, D.; Berlit, P. Phase Relationship between Cerebral Blood Flow Velocity and Blood Pressure. A Clinical Test of Autoregulation. *Stroke* **1995**, *26*, 1801–1804, doi:10.1161/01.str.26.10.1801.

37. Jamil, A.; Batsikadze, G.; Kuo, H.-I.; Meesen, R.L.J.; Dechent, P.; Paulus, W.; Nitsche, M.A. Current Intensity- and Polarity-Specific Online and Aftereffects of Transcranial Direct Current Stimulation: An FMRI Study. *Human Brain Mapping* **2020**, *41*, 1644–1666, doi:10.1002/hbm.24901.

38. Turner, D.A.; Degan, S.; Galeffi, F.; Schmidt, S.; Peterchev, A.V. Rapid, Dose-Dependent Enhancement of Cerebral Blood Flow by Transcranial AC Stimulation in Mouse. *Brain Stimulation* **2021**, *14*, 80–87, doi:10.1016/j.brs.2020.11.012.

39. Riddle, J.; Frohlich, F. Targeting Neural Oscillations with Transcranial Alternating Current Stimulation. *Brain Research* **2021**, *1765*, 147491, doi:10.1016/j.brainres.2021.147491.

40. Zhang, J.H.; Badaut, J.; Tang, J.; Obenaus, A.; Hartman, R.; Pearce, W.J. The Vascular Neural Network—a New Paradigm in Stroke Pathophysiology. *Nat Rev Neurol* **2012**, *8*, 711–716, doi:10.1038/nrneurol.2012.210.

41. Jolivet, R.; Coggan, J.S.; Allaman, I.; Magistretti, P.J. Multi-Timescale Modeling of Activity-Dependent Metabolic Coupling in the Neuron-Glia-Vasculature Ensemble. *PLOS Computational Biology* **2015**, *11*, e1004036, doi:10.1371/journal.pcbi.1004036.

42. Bozzo, L.; Puyal, J.; Chatton, J.-Y. Lactate Modulates the Activity of Primary Cortical Neurons through a Receptor-Mediated Pathway. *PLOS ONE* **2013**, *8*, e71721, doi:10.1371/journal.pone.0071721.

43. Mosienko, V.; Teschemacher, A.G.; Kasparov, S. Is L-Lactate a Novel Signaling Molecule in the Brain? *J. Cereb. Blood Flow Metab.* **2015**, *35*, 1069–1075, doi:10.1038/jcbfm.2015.77.

44. Workman, C.D.; Fietsam, A.C.; Ponto, L.L.B.; Kamholz, J.; Rudroff, T. Individual Cerebral Blood Flow Responses to Transcranial Direct Current Stimulation at Various Intensities. *Brain Sci* **2020**, *10*, E855, doi:10.3390/brainsci10110855.

45. Schmid, F.; Barrett, M.J.P.; Jenny, P.; Weber, B. Vascular Density and Distribution in Neocortex. *NeuroImage* **2019**, *197*, 792–805, doi:10.1016/j.neuroimage.2017.06.046.

46. Arora, Y.; Chowdhury, S.R.; Dutta, A. Physiological Neurovascular Modeling of Cerebrovascular Effects of Transcranial Electrical Current Stimulation. *Brain Stimulation: Basic, Translational, and Clinical Research in Neuromodulation* **2021**, *14*, 1597–1598, doi:10.1016/j.brs.2021.10.031.

47. Hansen, N. The CMA Evolution Strategy: A Tutorial 2016.

48. Glück, C.; Ferrari, K.D.; Binini, N.; Keller, A.; Saab, A.S.; Stobart, J.L.; Weber, B. Distinct Signatures of Calcium Activity in Brain Mural Cells. *eLife* **2021**, *10*, e70591, doi:10.7554/eLife.70591.

49. Moshkforoush, A.; Ashenagar, B.; Harraz, O.F.; Dabertrand, F.; Longden, T.A.; Nelson, M.T.; Tsoukias, N.M. The Capillary Kir Channel as Sensor and Amplifier of Neuronal Signals: Modeling Insights on K+-Mediated Neurovascular Communication. *PNAS* **2020**, *117*, 16626–16637, doi:10.1073/pnas.2000151117.

50. Tarantini, S.; Tran, C.H.T.; Gordon, G.R.; Ungvari, Z.; Csiszar, A. Impaired Neurovascular Coupling in Aging and Alzheimer's Disease: Contribution of Astrocyte Dysfunction and Endothelial Impairment to Cognitive Decline. *Exp Gerontol* **2017**, *94*, 52–58, doi:10.1016/j.exger.2016.11.004.

51. Moore, C.I.; Cao, R. The Hemo-Neural Hypothesis: On The Role of Blood Flow in Information Processing. *J Neurophysiol* **2008**, *99*, 2035–2047, doi:10.1152/jn.01366.2006.

52. Jindal, U.; Sood, M.; Dutta, A.; Chowdhury, S.R. Development of Point of Care Testing Device for Neurovascular Coupling From Simultaneous Recording of EEG and NIRS During Anodal Transcranial Direct Current Stimulation. *IEEE J Transl Eng Health Med* **2015**, *3*, 2000112, doi:10.1109/JTEHM.2015.2389230.

53. Nardo, D.; Creasey, M.; Negus, C.; Pappa, K.; Reid, A.; Josephs, O.; Callaghan, M.F.; Crinion, J.T. Transcranial Direct Current Stimulation with Functional Magnetic Resonance Imaging: A Detailed Validation and Operational Guide 2021.

54. Ekhtiari, H.; Ghobadi-Azbari, P.; Thielscher, A.; Antal, A.; Li, L.M.; Shereen, A.D.; Cabral-Calderin, Y.; Keeser, D.; Bergmann, T.O.; Jamil, A.; et al. A Checklist for Assessing the Methodological Quality of Concurrent TES-FMRI Studies (ContES Checklist): A Consensus Study and Statement. *Nat Protoc* **2022**, 1–24, doi:10.1038/s41596-021-00664-5.

55. Friston, K.J.; Fletcher, P.; Josephs, O.; Holmes, A.; Rugg, M.D.; Turner, R. Event-Related FMRI: Characterizing Differential Responses. *Neuroimage* **1998**, *7*, 30–40, doi:10.1006/nimg.1997.0306.

56. Vincent, T.; Badillo, S.; Risser, L.; Chaari, L.; Bakhous, C.; Forbes, F.; Ciuciu, P. Flexible Multivariate Hemodynamics FMRI Data Analyses and Simulations with PyHRF. *Front Neurosci* **2014**, *8*, 67, doi:10.3389/fnins.2014.00067.

57. Huang, Y.; Datta, A.; Bikson, M.; Parra, L.C. Realistic Volumetric-Approach to Simulate Transcranial Electric Stimulation—ROAST—a Fully Automated Open-Source Pipeline. *J. Neural Eng.* **2019**, *16*, 056006, doi:10.1088/1741-2552/ab208d.

58. Wu, G.-R.; Colenbier, N.; Van Den Bossche, S.; Clauw, K.; Johri, A.; Tandon, M.; Marinazzo, D. RsHRF: A Toolbox for Resting-State HRF Estimation and Deconvolution. *NeuroImage* **2021**, *244*, 118591, doi:10.1016/j.neuroimage.2021.118591.

59. Sancho, M.; Samson, N.C.; Hald, B.O.; Hashad, A.M.; Marrelli, S.P.; Brett, S.E.; Welsh, D.G. KIR Channels Tune Electrical Communication in Cerebral Arteries. *J Cereb Blood Flow Metab* **2017**, *37*, 2171–2184, doi:10.1177/0271678X16662041.

60. Mosayebi-Samani, M.; Jamil, A.; Salvador, R.; Ruffini, G.; Haueisen, J.; Nitsche, M.A. The Impact of Individual Electrical Fields and Anatomical Factors on the Neurophysiological Outcomes of TDCS: A TMS-MEP and MRI Study. *Brain Stimul* **2021**, *14*, 316–326, doi:10.1016/j.brs.2021.01.016.

61. Witthoft, A.; Em Karniadakis, G. A Bidirectional Model for Communication in the Neurovascular Unit. *J Theor Biol* **2012**, *311*, 80–93, doi:10.1016/j.jtbi.2012.07.014.

62. Dutta, A. Bidirectional Interactions between Neuronal and Hemodynamic Responses to Transcranial Direct Current Stimulation (TDCS): Challenges for Brain-State Dependent TDCS. *Front Syst Neurosci* **2015**, *9*, 107, doi:10.3389/fnsys.2015.00107.

63. Duffin, J.; Sobczyk, O.; McKetton, L.; Crawley, A.; Poublanc, J.; Venkatraghavan, L.; Sam, K.; Mutch, W.A.; Mikulis, D.; Fisher, J.A. Cerebrovascular Resistance: The Basis of Cerebrovascular Reactivity. *Front Neurosci* **2018**, *12*, doi:10.3389/fnins.2018.00409.

64. Bouma, G.J.; Muizelaar, J.P. Cerebral Blood Flow, Cerebral Blood Volume, and Cerebrovascular Reactivity after Severe Head Injury. *J Neurotrauma* **1992**, *9 Suppl 1*, S333-348.

65. Markus, H.; Cullinane, M. Severely Impaired Cerebrovascular Reactivity Predicts Stroke and TIA Risk in Patients with Carotid Artery Stenosis and Occlusion. *Brain* **2001**, *124*, 457–467, doi:10.1093/brain/124.3.457.

66. Bahr-Hosseini, M.; Bikson, M. Neurovascular-Modulation: A Review of Primary Vascular Responses to Transcranial Electrical Stimulation as a Mechanism of Action. *Brain Stimulation* **2021**, *14*, 837–847, doi:10.1016/j.brs.2021.04.015.

67. Jurcak, V.; Tsuzuki, D.; Dan, I. 10/20, 10/10, and 10/5 Systems Revisited: Their Validity as Relative Head-Surface-Based Positioning Systems. *NeuroImage* **2007**, *34*, 1600–1611, doi:10.1016/j.neuroimage.2006.09.024.

68. Rezaee, Z.; Kaura, S.; Solanki, D.; Dash, A.; Srivastava, M.V.P.; Lahiri, U.; Dutta, A. Deep Cerebellar Transcranial Direct Current Stimulation of the Dentate Nucleus to Facilitate Standing Balance in Chronic Stroke Survivors—A Pilot Study. *Brain Sciences* **2020**, *10*, 94, doi:10.3390/brainsci10020094.

69. Aasted, C.M.; Yücel, M.A.; Cooper, R.J.; Dubb, J.; Tsuzuki, D.; Becerra, L.; Petkov, M.P.; Borsook, D.; Dan, I.; Boas, D.A. Anatomical Guidance for Functional Near-Infrared Spectroscopy: AtlasViewer Tutorial. *Neurophotonics* **2015**, *2*, doi:10.1117/1.NPh.2.2.020801.

70. Jahani, S.; Setarehdan, S.K.; Boas, D.A.; Yücel, M.A. Motion Artifact Detection and Correction in Functional Near-Infrared Spectroscopy: A New Hybrid Method Based on Spline Interpolation Method and Savitzky–Golay Filtering. *Neurophotonics* **2018**, *5*, doi:10.1117/1.NPh.5.1.015003.

71. Friston, K.J.; Mechelli, A.; Turner, R.; Price, C.J. Nonlinear Responses in FMRI: The Balloon Model, Volterra Kernels, and Other Hemodynamics. *Neuroimage* **2000**, *12*, 466–477, doi:10.1006/nimg.2000.0630.

72. Florian, G.; Pfurtscheller, G. Elimination von Atmungseffekten Auf Bewegungsinduzierte Änderungen Der Herzrate - Elimination of Respiratory Effects on Movement-Induced Cardiac Response. **1997**, *42*, 203–206, doi:10.1515/bmte.1997.42.7-8.203.

73. Nitsche, M.A.; Paulus, W. Excitability Changes Induced in the Human Motor Cortex by Weak Transcranial Direct Current Stimulation. *J. Physiol. (Lond.)* **2000**, *527 Pt 3*, 633–639.

74. Steffener, J.; Tabert, M.; Reuben, A.; Stern, Y. Investigating Hemodynamic Response Variability at the Group Level Using Basis Functions. *Neuroimage* **2010**, *49*, 2113–2122, doi:10.1016/j.neuroimage.2009.11.014.

75. Tgavalekos, K.; Pham, T.; Krishnamurthy, N.; Sassaroli, A.; Fantini, S. Frequency-Resolved Analysis of Coherent Oscillations of Local Cerebral Blood Volume, Measured with near-Infrared Spectroscopy, and Systemic Arterial Pressure in Healthy Human Subjects. *PLOS ONE* **2019**, *14*, e0211710, doi:10.1371/journal.pone.0211710.

76. List, J.; Lesemann, A.; Kübke, J.C.; Külzow, N.; Schreiber, S.J.; Flöel, A. Impact of TDCS on Cerebral Autoregulation in Aging and in Patients with Cerebrovascular Diseases. *Neurology* **2015**, *84*, 626–628, doi:10.1212/WNL.0000000000001230.

77. Luckey, A.M.; McLeod, S.L.; Robertson, I.H.; To, W.T.; Vanneste, S. Greater Occipital Nerve Stimulation Boosts Associative Memory in Older Individuals: A Randomized Trial. *Neurorehabil Neural Repair* **2020**, *34*, 1020–1029, doi:10.1177/1545968320943573.

78. Fonteneau, C.; Mondino, M.; Arns, M.; Baeken, C.; Bikson, M.; Brunoni, A.R.; Burke, M.J.; Neuvonen, T.; Padberg, F.; Pascual-Leone, A.; et al. Sham TDCS: A Hidden Source of Variability? Reflections for Further Blinded, Controlled Trials. *Brain Stimul* **2019**, *12*, 668–673, doi:10.1016/j.brs.2018.12.977.

79. Dierkes, K.; Kassner, M.; Bulling, A. A Fast Approach to Refraction-Aware Eye-Model Fitting and Gaze Prediction. *ETRA* **2019**, doi:10.1145/3314111.3319819.

80. Hoeks, B.; Levelt, W.J.M. Pupillary Dilation as a Measure of Attention: A Quantitative System Analysis. *Behavior Research Methods, Instruments, & Computers* **1993**, *25*, 16–26, doi:10.3758/BF03204445.

81. Ozen, S.; Sirota, A.; Belluscio, M.A.; Anastassiou, C.A.; Stark, E.; Koch, C.; Buzsáki, G. Transcranial Electric Stimulation Entrains Cortical Neuronal Populations in Rats. *J. Neurosci.* **2010**, *30*, 11476–11485, doi:10.1523/JNEUROSCI.5252-09.2010.

82. Huang, W.A.; Stitt, I.M.; Negahbani, E.; Passey, D.J.; Ahn, S.; Davey, M.; Dannhauer, M.; Doan, T.T.; Hoover, A.C.; Peterchev, A.V.; et al. Transcranial Alternating Current Stimulation Entrains Alpha Oscillations by Preferential Phase Synchronization of Fast-Spiking Cortical Neurons to Stimulation Waveform. *Nat Commun* **2021**, *12*, 3151, doi:10.1038/s41467-021-23021-2.

83. Lewis, A.; Galetta, S. Editors' Note: Disruption of the Ascending Arousal Network in Acute Traumatic Disorders of Consciousness. *Neurology* **2020**, *95*, 233–233, doi:10.1212/WNL.0000000000010098.

84. Huntley, J.D.; Fleming, S.M.; Mograbi, D.C.; Bor, D.; Naci, L.; Owen, A.M.; Howard, R. Understanding Alzheimer's Disease as a Disorder of Consciousness. *Alzheimer's & Dementia: Translational Research & Clinical Interventions* **2021**, *7*, e12203, doi:10.1002/trc2.12203.

85. Harik, S.I.; Busto, R.; Martinez, E. Norepinephrine Regulation of Cerebral Glycogen Utilization during Seizures and Ischemia. *J Neurosci* **1982**, *2*, 409–414.

86. Monai, H.; Koketsu, S.; Shinohara, Y.; Ueki, T.; Kusk, P.; Hauglund, N.L.; Samson, A.J.; Nedergaard, M.; Hirase, H. Adrenergic Inhibition Facilitates Normalization of Extracellular Potassium after Cortical Spreading Depolarization. *Sci Rep* **2021**, *11*, 8150, doi:10.1038/s41598-021-87609-w.

87. Moheet, A.; Mangia, S.; Seaquist, E. Impact of Diabetes on Cognitive Function and Brain Structure. *Ann N Y Acad Sci* **2015**, *1353*, 60–71, doi:10.1111/nyas.12807.

88. Ocon, A.J. Caught in the Thickness of Brain Fog: Exploring the Cognitive Symptoms of Chronic Fatigue Syndrome. *Front Physiol* **2013**, *4*, 63, doi:10.3389/fphys.2013.00063.

89. Batsikadze, G.; Moliadze, V.; Paulus, W.; Kuo, M.-F.; Nitsche, M.A. Partially Non-Linear Stimulation Intensity-Dependent Effects of Direct Current Stimulation on Motor Cortex Excitability in Humans. *J Physiol* **2013**, *591*, 1987–2000, doi:10.1113/jphysiol.2012.249730.

90. Han, C.-H.; Song, H.; Kang, Y.-G.; Kim, B.-M.; Im, C.-H. Hemodynamic Responses in Rat Brain during Transcranial Direct Current Stimulation: A Functional near-Infrared Spectroscopy Study. *Biomed Opt Express* **2014**, *5*, 1812–1821, doi:10.1364/BOE.5.001812.

91. MacVicar, B.A.; Newman, E.A. Astrocyte Regulation of Blood Flow in the Brain. *Cold Spring Harb Perspect Biol* **2015**, *7*, doi:10.1101/cshperspect.a020388.

92. Monai, H.; Ohkura, M.; Tanaka, M.; Oe, Y.; Konno, A.; Hirai, H.; Mikoshiba, K.; Itohara, S.; Nakai, J.; Iwai, Y.; et al. Calcium Imaging Reveals Glial Involvement in Transcranial Direct Current Stimulation-Induced Plasticity in Mouse Brain. *Nat Commun* **2016**, *7*, 11100, doi:10.1038/ncomms11100.

93. Petzold, G.C.; Murthy, V.N. Role of Astrocytes in Neurovascular Coupling. *Neuron* **2011**, *71*, 782–797, doi:10.1016/j.neuron.2011.08.009.

94. Wachter, D.; Wrede, A.; Schulz-Schaeffer, W.; Taghizadeh-Waghefi, A.; Nitsche, M.A.; Kutschenko, A.; Rohde, V.; Liebetanz, D. Transcranial Direct Current Stimulation Induces Polarity-Specific Changes of Cortical Blood Perfusion in the Rat. *Exp. Neurol.* **2011**, *227*, 322–327, doi:10.1016/j.expneurol.2010.12.005.

95. Mielke, D.; Wrede, A.; Schulz-Schaeffer, W.; Taghizadeh-Waghefi, A.; Nitsche, M.A.; Rohde, V.; Liebetanz, D. Cathodal Transcranial Direct Current Stimulation Induces Regional, Long-Lasting Reductions of Cortical Blood Flow in Rats. *Neurol. Res.* **2013**, *35*, 1029–1037, doi:10.1179/1743132813Y.0000000248.

96. Karanth, S.S.; Mujumdar, R.; Sahoo, J.P.; Das, A.; Stachowiak, M.K.; Dutta, A. Human Brain Organoid Platform for Neuroengineering Optical Theranostics in Neonatal Sepsis. In Proceedings of the Converging Clinical and Engineering Research on Neurorehabilitation IV; Torricelli, D., Akay, M., Pons, J.L., Eds.; Springer International Publishing: Cham, 2022; pp. 753–757.

97. Krause, B.; Cohen Kadosh, R. Not All Brains Are Created Equal: The Relevance of Individual Differences in Responsiveness to Transcranial Electrical Stimulation. *Frontiers in Systems Neuroscience* **2014**, *8*.

98. Kathuria, A.; Lopez-Lengowski, K.; Jagtap, S.S.; McPhie, D.; Perlis, R.H.; Cohen, B.M.; Karmacharya, R. Transcriptomic Landscape and Functional Characterization of Induced Pluripotent Stem Cell–Derived Cerebral Organoids in Schizophrenia. *JAMA Psychiatry* **2020**, *77*, 745–754, doi:10.1001/jamapsychiatry.2020.0196.

99. Zhang, L.; Su, F.; Buizer, S.; Lu, H.; Gao, W.; Tian, Y.; Meldrum, D. A Dual Sensor for Real-Time Monitoring of Glucose and Oxygen. *Biomaterials* **2013**, *34*, 10.1016/j.biomaterials.2013.09.031, doi:10.1016/j.biomaterials.2013.09.031.

100. Tong, L.; Hill, R.A.; Damisah, E.C.; Murray, K.N.; Yuan, P.; Bordey, A.; Grutzendler, J. Imaging and Optogenetic Modulation of Vascular Mural Cells in the Live Brain. *Nat Protoc* **2021**, *16*, 472–496, doi:10.1038/s41596-020-00425-w.